

PLUTO: Pathology-Universal Transformer

Dinkar Juyal¹, Harshith Padigela¹, Chintan Shah¹, Daniel Shenker², Natalia Harguindeguy², Yi Liu³, Blake Martin³, Yibo Zhang³, Michael Nercessian³, Miles Markey³, Isaac Finberg³, Kelsey Luu³, Daniel Borders³, Syed Ashar Javed³, Emma Krause³, Raymond Biju, Aashish Sood, Allen Ma, Jackson Nyman, John Shamshoian, Guillaume Chhor, Darpan Sanghavi, Marc Thibault, Limin Yu, Fedaa Najdawi, Jennifer A. Hipp, Darren Fahy, Benjamin Glass, Eric Walk, John Abel, Harsha Pokkalla, Andrew H. Beck, and Sean Grullon^{*4}

¹Project Lead and Co-lead author

²Workstream Lead

³Core Team

⁴Directional Lead
PathAI

Abstract

Pathology is the study of microscopic inspection of tissue, and a pathology diagnosis is often the medical gold standard to diagnose disease. Pathology images provide a unique challenge for computer-vision-based analysis: a single pathology Whole Slide Image (WSI) is gigapixel-sized and often contains hundreds of thousands to millions of objects of interest across multiple resolutions.

In this work, we propose PathoLogY Universal Transformer (PLUTO): a light-weight pathology FM that is pre-trained on a diverse dataset of 195 million image tiles collected from multiple sites and extracts meaningful representations across multiple WSI scales that enable a large variety of downstream pathology tasks. In particular, we design task-specific adaptation heads that utilize PLUTO’s output embeddings for tasks that span pathology scales ranging from subcellular to slide-scale, including instance segmentation, tile classification, and slide-level prediction. We compare PLUTO’s performance to other state-of-the-art methods on a diverse set of external and internal benchmarks covering multiple biologically relevant tasks, tissue types, resolutions, stains, and scanners. We find that PLUTO matches or outperforms existing task-specific base-

lines and pathology-specific foundation models, some of which use orders-of-magnitude larger datasets and model sizes when compared to PLUTO. Our findings present a path towards a universal embedding to power pathology image analysis, and motivate further exploration around pathology foundation models in terms of data diversity, architectural improvements, sample efficiency, and practical deployability in real-world applications.

1. Introduction

Pathology as a medical discipline is instrumental in providing diagnostic and prognostic information to clinicians and patients. In a pathology workflow, surgical tissue specimens are collected, stained, and fixed for microscopy. Microscopic analysis of the tissue is used to establish a diagnosis, estimate disease severity, and identify relevant clinical features for treatment [20, 39, 55].

The practice of pathology is not inherently digital; traditionally, pathology slides are manually examined under a microscope. Microscopy slides are increasingly being digitized in their entirety via slide scanning, generating digital whole slide images (WSIs or slides). While WSIs provide a wealth of information about a specimen to trained readers such as pathologists, the images themselves are enormous. Each WSI contains up to millions of cells and can be gigapixels in scale, making an exhaustive quantitative manual analysis of WSIs nearly impossible. In addition, information for making pathologic decisions or classifications may

*Corresponding Author: sean.grullon@pathai.com

The authors would like to thank Jon Ross, Elliot Miller, Alfred Eng and Maximillian King for their MLOps support, Jacqueline Brosnan-Cashman for her help with illustrations and thank Vincent Billaut and Michael Griffin for their manuscript feedback

exist at multiple scales, from several μm to several cm, complicating analysis.

Artificial intelligence (AI) and machine learning (ML) techniques are well-suited for the quantitative study of these extremely large WSIs. A wide variety of ML techniques have been developed and applied to the pathology domain, ranging from detection and characterization of microscopic biological entities within the WSI, to end-to-end frameworks for making slide-level predictions or diagnoses [5–7, 9, 17, 31, 56].

However, developing supervised machine learning models for pathology comes with many challenges [52]. These algorithms need large amounts of labeled data which is often expensive to collect and in some cases hard to source due to the low prevalence of disease characteristics. Additionally, these models need to generalize across variations introduced by source sites, scanners, and staining procedures [25, 37, 42, 49]. Lowering the data burden and improving the robustness of these models is important for broad-scale adoption of AI models in pathology practice. Furthermore, the diversity of individual tasks in pathology (such as classification, segmentation, and slide-level prediction) makes training bespoke AI models from scratch challenging.

Foundation models [50] (FMs) are large scale deep-learning models often pre-trained on broad-scale, unlabeled data using self-supervision and can be adapted to multiple downstream tasks [43, 44] such as image classification and object detection with fewer labels than traditional strongly-supervised methods [3]. This adaptation procedure normally involves utilizing the representation (also referred to as embeddings) produced by a pre-trained FM *backbone* to fine-tune a task head (with significantly fewer model parameters than the backbone) on a particular downstream task.

1.1. Previous Pathology Foundation Models

FMs are promising for pathology as they can take advantage of large amounts of unlabeled data to build rich representations which can be easily adapted for downstream tasks in a data-efficient manner. The diversity of pre-training data results in these models generating robust representations, enabling them to generalize better than individual task-specific models trained on smaller datasets [50].

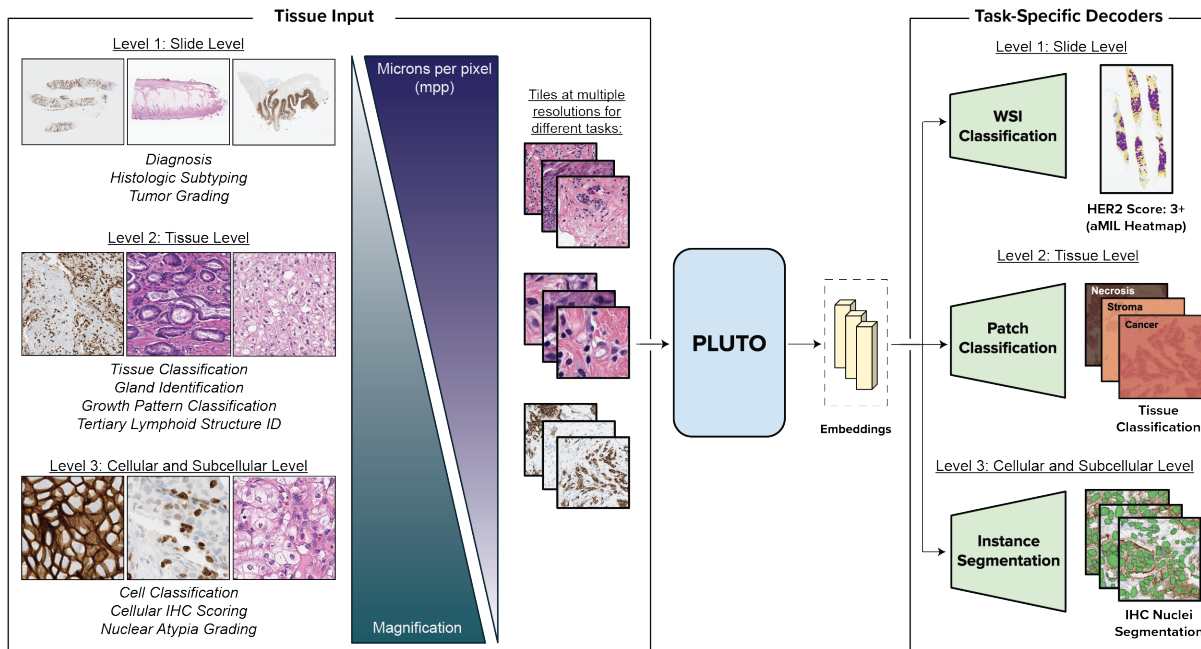
Additionally, sharing a backbone across different tasks could also reduce the development and maintenance overhead associated with bespoke task-specific models. Given this prospect, the computational pathology community has made rapid progress in applying self-supervised techniques that have shown promise on natural images such as DINO [8], iBOT [58], and DINOv2 [44] to pathology. Most of these efforts have relied on pre-training with a large amount of proprietary data and scaling up the number of backbone parameters used in order to demonstrate high performance

on various downstream tasks including tissue classification, disease subtyping classification, and cancer histology segmentation.

Kang *et al.* [32] have compared a panel of self-supervised learning strategies on tile classification of tissue types and cell segmentation, and have reported that the backbone trained with the DINO [8] vision transformer backbone demonstrated superior performance. Filiot *et al.* have developed Phikon [21] based on the iBOT [58] self-supervised strategy, relying on public data from The Cancer Genome Atlas (TCGA) [51], and evaluated their model on tissue type tile classification and weakly-supervised slide-level cancer subtyping. Shaikovski *et al.* have developed Virchow [54] based upon the DINOv2 vision transformer (ViT) [19] backbone, and trained the model at scale with two billion tiles corresponding to 1.5 million WSIs from the Memorial Sloan Kettering Cancer Center (MSKCC). This model has been evaluated on a tile classification task across 17 different cancer types including seven rare cancer types, and has also demonstrated high performance on slide-level biomarker prediction tasks. Winterhoff *et al.* have developed RudolfV [18], also based on DINOv2 pre-training and relied on both public data from TCGA and proprietary data. Winterhoff *et al.* have reported tissue tile classification results across six public datasets and cell segmentation benchmarks on their proprietary test set. UNI [10] from Chen *et al.* also used a DINOv2 backbone, but introduced additional data diversity through the “Mass-100K” dataset which was sourced from Massachusetts General Hospital (MGH), Brigham and Women’s Hospital, and the Genotype–Tissue Expression (GTEx) consortium. UNI has been adapted to a wider variety of tasks in addition to tissue classification, including disease subtyping classification and cancer histology segmentation.

Despite the encouraging results from these pathology FMs, there are several areas of improvement that would further drive the adoption of FMs in pathology practice. First, FM pre-training has predominantly relied on a large amount of proprietary data from a single site. There are site-specific batch effects [29] in WSIs arising from site-specific variation, including both stain and the patient population, which can lower the robustness of AI models when unaccounted for. Additionally, a lack of pixel-level annotations at scale can limit the downstream performance of these pathology FMs as recent studies [26] have demonstrated the importance of data and label diversity in self-supervised pre-training. Our large network of pathologists has gathered millions of pixel level annotations [16], which provided us with a powerful source of data to drive FM improvements. Second, the architectural design of pathology FMs could further take advantage of the multi-scale nature of WSIs outlined in Section 2.1. Finally, FM backbones have often been trained with a large number of model pa-

A. PLUTO framework for multi-resolution pathology tasks



B. PLUTO training paradigm

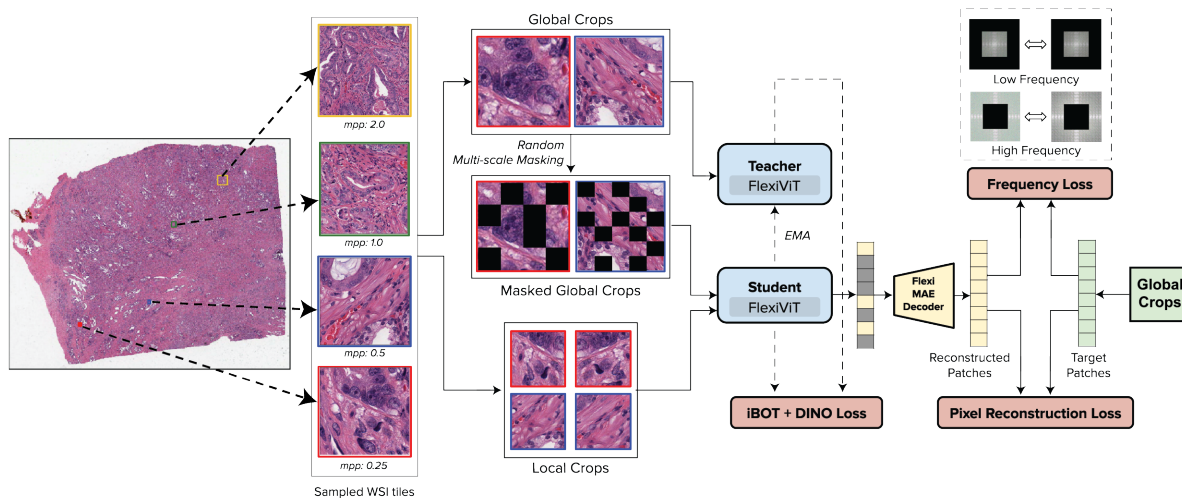


Figure 1. Overview of PLUTO. Panel A) outlines the PLUTO multi-resolution adaptation pipeline. Tiles are extracted from WSIs at multiple resolutions and correspond to scales that capture different biological contexts. We organize pathology tasks according to these biological contexts as slide level, tissue level, and cellular & subcellular level tasks, respectively. PLUTO generates embeddings that are task-agnostic and can be used in a variety of downstream tasks, where adaptation to WSI-level prediction, tile classification, and instance segmentation are shown. Panel B) demonstrates the PLUTO architecture in detail. WSI tiles at multiple resolutions are masked with varying patch sizes and passed to the backbone for self-supervised pre-training. The architecture is optimized for flexibility across multiple scales and patch sizes. In addition to DINO and iBOT losses, MAE and Fourier losses are applied across varying mask sizes to control the amount of low- and high-frequency information that is preserved.

rameters, which increases the complexity and cost of deploying these models and hence limits their practical use in routine pathology practice.

1.2. Our Approach

We designed and built the *PathoLogy-Universal Transformer*, or PLUTO, a state-of-the-art pathology foundation model that, inspired by the dwarf planet, is based on a novel light-weight ViT backbone that is pre-trained on a diverse dataset from multiple sites and extracts meaningful representations across the levels of the WSI pyramid outlined in Section 2.1. The key features of PLUTO, namely the pre-training dataset, architecture, multi-scale task evaluation, and deployability, are outlined below:

1. **Pre-training Dataset** We compiled a large dataset across a diverse spectrum of histology stains, scanners, and biological objects across resolution scales that include 200+ biologically-meaningful objects and region types (which we term *substances*) from more than 50 sources (Section 2.2).
2. **Architecture** We designed the PLUTO backbone to generate informative feature representations at different length scales from a compact ViT backbone. We achieved this by implementing a self-supervised learning scheme that accommodates flexible patch sizes from the FlexiViT scheme [4], extending it to accommodate multiple magnifications during training, and modifying the DINOv2 loss by adding a Masked Autoencoder (MAE) [28] objective and a Fourier-loss-based term to modulate the preservation of low- and high-frequency components (Section 3.1).
3. **Multi-scale Evaluation** We evaluated the quality of the resulting FM by constructing a suite of adaptation heads to perform diverse, challenging tasks across the levels of the WSI pyramid (Sections 2.1, 3.3), and evaluated performance across different biologically-relevant benchmarks (Section 4).
4. **Deployability.** Performing a computational pathology task may require embedding tens to hundreds of thousands of WSI tiles to make a single prediction. To enable this, we focused on developing a model that was efficient (Section 4.4).

2. Pathology Task Hierarchy and Pre-training Dataset

2.1. Pyramid Structure of Whole Slide Images

WSIs are digitized and stored in a multi-scale pyramidal structure, where the base of the pyramid is the highest-resolution image data as captured by the slide scanner. The resulting scan of a WSI can reach $200,000 \times 200,000$ pixels at a full resolution of 0.25 microns (μm) per pixel (mpp)

[46]; however, different “levels” of the pyramid may be accessed for different purposes.

Biological entities observed on WSIs vary dramatically in scale, and therefore pathologists will commonly move between magnifications to assess different aspects of a tissue sample on a pathology slide [41]. At low magnification, pathologists may scan across slides to identify regions of interest in the tissue, with characteristic lengths of approximately 1 mm–1 cm. At middle magnification (such as 5–10 \times) pathologists commonly view structures at length scales of 200 μm –1 mm. At this scale, pathologists distinguish between tissue types, glands, tumor growth patterns, histologic subtypes of diseases, or other multicellular entities in the image. At high magnification (20–40 \times) it is possible to resolve entities 1 μm –50 μm in length, such as individual cell identities, subcellular structural morphology used in determining malignancy, or localization of immunohistochemical (IHC) staining [40].

The hierarchical nature of biological entities necessitates considering the multiple scales at which information must be extracted and used by ML algorithms. For example, passing a 224×224 image tile at 0.25 mpp through an encoder developed for encoding at 1 mpp may completely miss relevant nuclear pleomorphism, whereas passing a 224×224 tile at 1 mpp through an encoder developed for encoding at 0.25 mpp may be unable to adequately distinguish between acinar and lepidic growth patterns. For clarity, we organize pathology tasks according to such biological scales as follows:

- **Level 1: Slide Level** This scale includes tasks that label the entire slide such as predicting driver gene mutations in cancer, histologic subtyping, or tumor grading. However, it is uncommon that slide-level assessments are made at slide-level magnification. Typically, assessments made at this scale are aggregated across evaluation of higher-magnification tiles.
- **Level 2: Tissue Level** This is the scale at which it is possible to identify and characterize tissue regions (e.g. cancer regions and necrotic regions) and many-cellular objects such as glands.
- **Level 3: Cellular and Subcellular Level** This is typically the maximal resolution of a WSI, where cellular and subcellular morphology is evident.

2.2. Pre-training Data Characteristics

The dataset used for self-supervised pre-training comprises public and proprietary datasets, totaling 195M image tiles sampled at four resolutions from 158,852 WSIs derived from over 50 source sites (Figure 2). The WSIs span over 16 tissue groups (Table 4) and 28 disease areas (Table 7), which capture a broad range of benign, malignant, and inflammatory lesions. Additionally, the training set is unique in the representation covering 11 scanners and

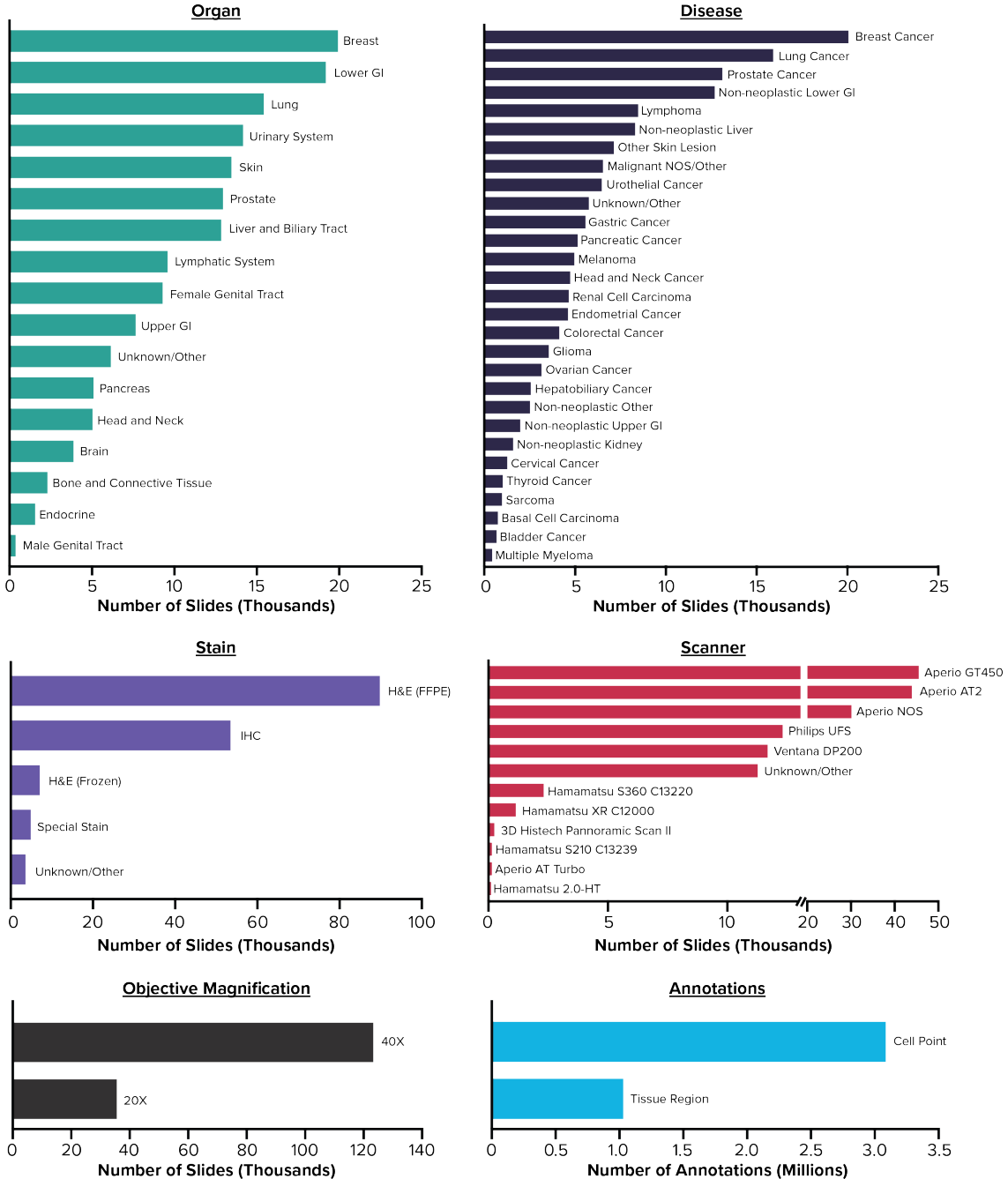
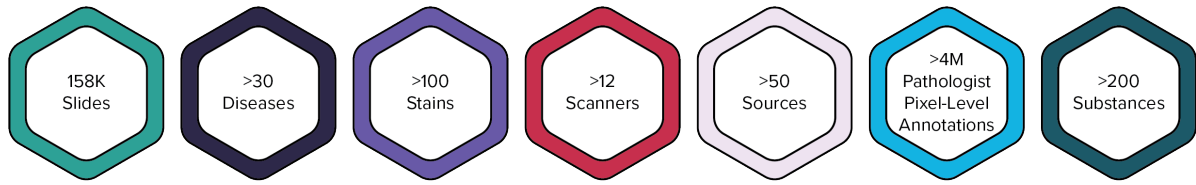


Figure 2. Dataset characterization for the pre-training dataset. The distribution of the dataset by organ, disease, stain, scanner, and objective magnification is shown, as well as the distribution of cell point and tissue region annotations which augment the pre-training dataset (NOS: Not Otherwise Specified). Aggregate data characteristics are summarized above these distributions which also indicate the number of biologically-meaningful objects and region types, which we term *substances* (e.g. lymphocyte, blood vessel, Gleason pattern 3 prostate cancer, tumor bed). The large number of source sites (50+) guarantees large diversity during PLUTO self-supervised pre-training.

four stain groups: hematoxylin and eosin (H&E) formalin-fixed paraffin-embedded (FFPE), H&E frozen, IHC (capturing over 100 distinct IHC stains including PD-L1, HER2, and Ki-67) and special stains (including six stains such as trichrome and iron) (Tables 5, 8). The base objective magnification of our training set consists of both 20 \times and 40 \times slides (Table 6).

Prior to tile sampling, we identify usable tissue regions using ArtifactDetect [45], a ResNet-style convolutional neural network trained to segment usable tissue, artifact, and background. This model provides significant performance gains for usable tissue identification in our experience compared to other methods such as Otsu masking in terms of generalization across different stains, scanners, diseases, and organs. Tiles are sampled from regions of usable tissue at up to four different resolutions: 40 \times (0.25 mpp), 20 \times (0.5 mpp), 10 \times (1 mpp), and 5 \times (2 mpp).

Following findings from DINOv2 [44] highlighting the significant value of incorporating curated data into self-supervised pre-training, this dataset is augmented with an additional set of samples extracted from over four million manual annotations from board-certified pathologists. These hand-drawn pathologist annotations correspond to hundreds of different types of biological entities at various scales (e.g., lymphocyte, blood vessel, Gleason pattern 3 prostate cancer, tumor bed). During pre-training, the labels are discarded, but the inclusion of pathologist-curated regions covering a wide range of biological patterns provides an implicit data diversity in the pre-training process. This source of biological diversity, combined with the broad range of stains, organs, diseases, and source sites, makes this one of the most diverse large-scale digital pathology datasets to date.

3. Methods

3.1. PLUTO Architecture Overview

PLUTO (Figure 1) is designed with specific characteristics in mind to enable its usage on a wide range of use-cases, as described in Section 1.2. To design the PLUTO architecture, we start from DINOv2 [44] which combines DINO [8] and iBOT [58] losses (along with KoLeo regularizer) to learn relevant representations at the tile and patch levels respectively. Note, we use **tile** and **image** interchangeably to refer to the image tiles and **patches** to refer to the patch-tokens obtained by dividing the tile into smaller patches for processing in ViTs. The DINOv2 architecture was primarily developed for natural images that are often object-centric. Pathology WSI tiles on the other hand have thousands of objects such as nuclei, cells, and glands with different sizes, observed at different image resolutions (Section 2.1). To design an encoder which can capture details of objects at different levels of granularity, we add in a MAE [28]

objective with multi-scale masking. The MAE setup tries to reconstruct masked regions of the input image (often a large fraction of the input) from the unmasked regions. We perform masking by varying the patch sizes used for masking while using images across different resolutions of the WSI as shown in Figure 1. In addition to the pixel-level reconstruction loss used in MAE, we add a Fourier reconstruction loss to control the amount of low- and high-frequency information preserved during the pre-training process.

To enable the encoder and decoder to handle varying patch sizes for multi-scale masking, we employ the FlexiViT setup [4]. Since patch size controls the granularity of information captured by the encoder, different downstream tasks may need different patch sizes for optimal performance. The FlexiViT setup allows us to adapt the same backbone to different tasks without needing to train a backbone for every patch size. The patch size also determines the effective sequence length used in ViTs and FlexiViT allows us to cater to different compute budgets by selecting the most suitable patch size at inference time.

3.2. PLUTO Backbone Training

We extract images from the dataset described in Section 2.2, with the image resolution selected randomly (with pre-specified probabilities). Two global crops and four local crops of sizes 224 and 96 respectively are taken from each image, consistent with DINOv2 training. The local crops are passed to the student, while the global crops are passed to the teacher. The teacher’s weights are updated using an exponential moving average of the student’s weights rather than backpropagation. The crops provided to the student are randomly masked for the iBoT objective. Meanwhile, a separate masking setup with a higher masking ratio is applied to the global crops for the MAE objective. The mask sizes are consistent with the patch sizes which are dynamically chosen from [8, 16, 32] to enable multi-scale masking. The flexible patch embedding step ensures that the architecture can accommodate patches of variable sizes. Since a vanilla MAE decoder cannot work with variable sized masks due to the presence of linear layers, a similar “flexification” setup is added to the MAE decoder to generate reconstructions with variable mask sizes. Learnable position embeddings are used in the MAE decoder. L2-norm loss between the reconstructed and the original image is used for the MAE objective.

Beyond the original MAE objective, we decompose the reconstructed image into its low- and high-frequency components. This decomposition is crucial for addressing distinct aspects of image quality that are captured in different frequency ranges. To achieve this, the Fourier spectrum of the reconstructed image is dissected into low- and high-frequency bands using a set of low-pass and high-pass filters. By applying these filters, the method effectively iso-

lates the components of the image that represent basic structures and details (low frequency) from those encapsulating finer details and textures (high frequency). After this separation, the L2 loss is computed independently for both the low- and high-frequency parts of the image. This bifurcated approach allows for a more nuanced adjustment and optimization of the reconstructed image by applying tunable weights to the losses from each frequency band before their aggregation. The sum of these weighted losses forms the overall Fourier reconstruction loss, which the training process aims to minimize [57]. The whole loss function $\mathcal{L}(\hat{y}, y)$ is listed in Eq. (1) and the detailed Fourier loss $\mathcal{L}_{\text{Fourier}}(\hat{y}, y)$ is listed in Eq. (2). \hat{y} represents the masked regions of the predicted image and y represents the masked regions of the ground truth image. The Discrete Fourier Transform (DFT) is denoted by \mathcal{F} . The mask M in the Fourier space acts as a low-pass filter, and $1 - M$ acts as a high-pass filter. The weights λ_1 and λ_2 are used to balance the contributions of the low-pass and high-pass filtered errors, respectively. The value of λ_1 is set to 5 and λ_2 is set to 1. The weights of other losses are set to 1. $\|\cdot\|_2$ denotes the L2 loss.

$$(1) \quad \mathcal{L}(\hat{y}, y) = \mathcal{L}_{\text{DINO}}(\hat{y}, y) + \mathcal{L}_{\text{iBOT}}(\hat{y}, y) \\ + \mathcal{L}_{\text{MAE}}(\hat{y}, y) + \mathcal{L}_{\text{Fourier}}(\hat{y}, y)$$

$$(2) \quad \mathcal{L}_{\text{Fourier}}(\hat{y}, y) = \lambda_1 \cdot \|M \cdot \mathcal{F}(\hat{y}) - M \cdot \mathcal{F}(y)\|_2^2 \\ + \lambda_2 \cdot \|(1 - M) \cdot \mathcal{F}(\hat{y}) - (1 - M) \cdot \mathcal{F}(y)\|_2^2$$

We observe slightly better performance with the teacher over the student, and thus use the teacher for all downstream tasks.

We use ViT-S for the student and teacher encoders, and a shallower model is used for the MAE decoder. For training, we use AdamW with a base learning rate of 0.002 and a learning rate warmup for the first 5 epochs. We use a distributed training setup to scale the training across 64 NVIDIA A40 GPUs.

3.3. PLUTO Adaptation

The backbone training process outlined above learns generic, task- features. In order to leverage its general capabilities, we add task-specific heads and *adapt* these heads through supervised fine-tuning, while keeping the backbone fixed, or frozen. This adaptation process is efficient and provides the flexibility to use the same pre-trained backbone for specialized tasks across the biological scales described in Section 2.1. Although different tasks may require the use of different patch sizes to capture relevant context, the FlexiVit setup allows us to dynamically select the backbone patch size for adaptation.

In this section we describe the techniques underlying the specialized task heads that work across these biological scales. At Level 1, we adapt PLUTO to slide-level

classification tasks with a multiple-instance learning (MIL) head, further discussed in Section 3.3.1. We adapt PLUTO to tissue-level (Level 2) & cellular- and subcellular-level (Level 3) biological scales, respectively, through the tile-level classification and instance segmentation task heads that we further describe in Section 3.3.2. The overall architecture is illustrated in panel B of Figure 1.

3.3.1 Slide-level Task Adaptation

We adapt PLUTO to Level 1 slide-level tasks described in Section 2.1 by performing weak supervision on slide-level labels. In particular, MIL [30] is a weakly supervised learning technique where sets of instances are grouped into a “bag” and used to learn bag-level labels. These MIL models consist of three parts: (1) a featurizer which generates representations of each image tile in a bag, (2) an aggregation module which combines tile representations using a permutation-invariant function (typically attention) to generate a bag-level representation, and (3) a classifier which outputs a bag-level prediction. We adapt our FM backbones by using the pre-trained backbones directly as featurizers, with the adaptation heads (which are the downstream components consisting of an attention module and classifier layer) operating on the feature vectors generated from these backbones. These models are trained with the featurizer either frozen (FZ) or unfrozen (FT, or fine-tuned) during MIL training. We use the AdditiveMIL classifier [31], which enables interpretable model predictions and class-wise heatmaps.

3.3.2 Tissue-level, Cellular- and Subcellular-level Task Adaptation

We adapt PLUTO to tissue-level and cellular/subcellular-level biological scales through fine-tuning either a tile classification or an instance segmentation adaptation head. These two adaptation strategies are informed by the availability of labeled data: tile-level classification only requires labels at the image tile level, whereas instance segmentation requires pixel-level annotations.

We explore and benchmark a range of adaptation head architectures for tile classification, ranging from single linear layers to multilayer perceptrons (MLPs) with different pooling strategies. By incorporating domain-specific knowledge from histopathology tiles, the aim is to develop a light-weight adaptation head that identifies critical features captured in the backbone embeddings of these tiles, such as cellular morphology and tissue region characteristics. This allows for the classification of tiles into various categories, such as healthy tissue or cancerous tissue regions.

In the analysis of gigapixel histopathology slides, such tile-level classification tasks can be effective substitutes for segmentation, a task which presents significant challenges

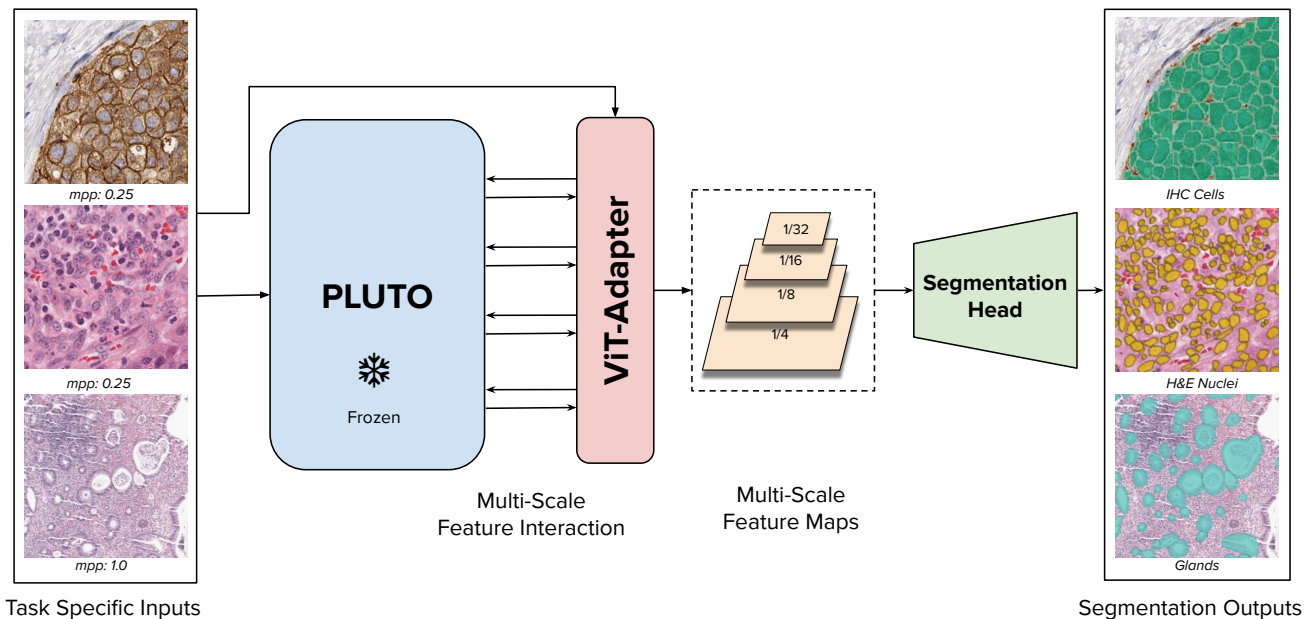


Figure 3. Instance segmentation adaptation with PLUTO. In this figure, we demonstrate example task-specific inputs and outputs using the frozen PLUTO backbone, and our segmentation adaptation approach on top using an adapter that outputs maps at varying spatial and semantic resolutions, followed by a segmentation head to generate instance segmentation masks. We demonstrate that our approach works across object scales from nuclei (top two images) to glands (bottom) and across stain types. In our proprietary datasets, Gland segmentation is trained at 768×768 at 1 mpp whereas nuclei segmentation is at 384×384 at 0.25 mpp. In our public benchmark experiments, we follow the prescribed task setup.

in terms of collecting exhaustive, high-quality annotations. However, morphological descriptors of nuclei, cells, glands, vessels, and other biological entities are crucial prognostic indicators for various pathological analyses. Therefore, we developed specialized task heads designed for instance segmentation, enhancing our ability to effectively analyze and interpret these critical features.

We adapt the SSL-pre-trained ViT backbone to instance segmentation tasks via two distinct frameworks: Mask R-CNN [27] and Mask2Former [13], as illustrated in Figure 3. While Mask R-CNN relies on region proposals and conventional mechanisms such as non-maximum suppression, Mask2Former employs a transformer-based approach, leveraging object queries to generate instance segmentation results, a methodology that presents a compelling advantage for our purposes since it does not rely on hand-tuned region proposals. To the best of our knowledge, this is the first work comparing Mask2Former to ViT + Mask R-CNN approaches on histopathology tasks. We also experimented with combining the ViT with a ViT-Adapter [12], which has been shown to improve segmentation performance. The output feature maps of the adapter, corresponding to different spatial resolutions of the input image, are used as the input to Mask R-CNN and Mask2Former.

We report the performance of these adaptation ap-

proaches on both proprietary datasets and public datasets, as we present in Section 4. We evaluate our adaptation techniques on our proprietary datasets with the object detection F1, semantic segmentation F1 and Aggregated Jaccard Index (AJI) [36] metrics. We evaluate our methods on public datasets with the metrics as originally defined in those public benchmarks.

4. Results

We evaluate the effectiveness of adapting PLUTO for tasks across biological scales corresponding to the pyramid levels of a WSI outlined in Section 2.1. A summary list of all benchmarks is given in Table 1.

4.1. Slide-level Results

4.1.1 Slide-level Datasets

We consider two slide-level prediction tasks for evaluating our backbone. The first is the prediction of the cancer subtypes Adenocarcinoma and Squamous cell carcinoma in non-small cell lung carcinoma (NSCLC) H&E-stained WSIs, a popular benchmark for slide-level evaluation. The second is the quantification of the HER2 biomarker across four scores (0, 1+, 2+, 3+) in IHC-stained breast cancer slides, which measures the expression level of the HER2

Task Level	Source	Benchmark Name	Task Type	# Samples	# Classes	Resolution	Patch Size
Slide	Public	NSCLC subtyping [51]	WSI-level Classification	500	2	0.5 mpp	16
Tissue	Public	H&E CRC-100K [34]	Tile Classification	107,180	9	0.5 mpp	16
Tissue	Public	Camelyon17-WILDS [35]	Tile Classification	455,954	2	1 mpp	16
Tissue	Public	GlaS [48]	Instance Segmentation	165	2	0.465 mpp	16
Cell	Public	PanNuke [22]	Instance Segmentation	481	5	0.25 mpp	16
Slide	Proprietary	HER2 Scoring	WSI-level Classification	500	4	0.5 mpp	16
Tissue	Proprietary	H&E Pan-Onc. Tissue	Tile Classification	196,807	4	0.5 mpp	16
Tissue	Proprietary	IHC Pan-Onc. Tissue	Tile Classification	196,807	4	0.5 mpp	16
Tissue	Proprietary	H&E IBD Tissue	Tile Classification	648,794	10	0.5 mpp	16
Tissue	Proprietary	H&E Glands	Instance Segmentation	518	2	1 mpp	8, 16, 32
Cell	Proprietary	H&E Pan-Onc. Cell	Tile Classification	212,036	9	0.5 mpp	8
Cell	Proprietary	IHC Cell	Instance Segmentation	225	2	0.25 mpp	8, 16
Cell	Proprietary	IHC and H&E Nuclei	Instance Segmentation	216	2	0.25 mpp	8, 16

Table 1. Summary overview of PLUTO benchmarks. The benchmarks cover the range of pyramid levels in WSIs, as well as resolutions and task types. The variety of tasks demonstrates the adaptability of the pre-trained PLUTO embeddings. Patch Size denotes the FlexiViT patch size used for that downstream task.

protein and is clinically relevant for targeted patient therapy [53].

For NSCLC subtyping, we use slides from the publicly available TCGA Adenocarcinoma (LUAD) and Squamous Cell Carcinoma (LUSC) groups. We use 500 slides for model development and 247 (128 LUAD / 119 LUSC) slides for test set evaluation. We evaluate out-of-distribution (OOD) performance using a proprietary dataset of 205 WSIs (162 Adenocarcinoma WSIs, 45 Squamous Cell Carcinoma WSIs) collected from a different source site with varying image acquisition and processing steps, resulting in visual differences from the TCGA WSIs. Since slide-level prediction tasks are often limited by the number of slides available for development, we limit our development set to 500 slides for both of these tasks and evaluate model performance on in-distribution (ID) and OOD test sets.

For HER2 scoring we use slides from an internal dataset constructed from multiple source sites, scanners and stain clones. We use 500 slides for model development and 250 slides with similar sample characteristics for ID evaluation. For OOD evaluation we use 229 slides collected from two held-out source sites with different sample characteristics.

4.1.2 Slide-level Results

We compare our PLUTO pre-trained backbones against both pathology and ImageNet pre-trained baselines. We compare against an ImageNet pre-trained CNN-based backbone (ShuffleNet) [38], as well as Meta-DINOv2 ViT-S pre-trained on ImageNet [44]. During MIL training, the ViT-S based models are trained with frozen featurizers (FZ), and the PLUTO backbone is evaluated with a FlexiViT patch size of 16. CNN-based models are trained with both frozen (FZ) and fine-tuned (FT) featurizers due to the smaller backbone size.

We use macro-F1 and AUROC for evaluating the ID and OOD performance for both datasets. The metrics are computed using 1,000 bootstrapped runs, reporting the mean and standard deviation. Results of these experiments are reported in Table 2. The pathology pre-trained backbones are the best performing on the ID test sets.

In the case of NSCLC, the OOD slides exhibit distinct characteristics compared to the ID TCGA slides. As a result, all models experience a decrease in performance. However, PLUTO experiences a comparatively smaller drop and emerges as the top performer among them. On HER2, the performance between ID and OOD datasets is more comparable, and PLUTO performs better compared to all backbones, including the fine-tuned ShuffleNet. We use AdditiveMIL [31] to generate heatmaps to identify regions on the slide corresponding to different HER2 scores. We show examples comparing the heatmaps with ground truth ROIs in Figure 4.

4.2. Tissue-level Results

4.2.1 Tile Classification: Public Datasets

We used two publicly available datasets: CRC-100K [34] and Camelyon17-WILDS [2, 35]. The CRC-100K dataset consists of 107,180 images (224×224 at 0.5 mpp) of human colorectal cancer (CRC) and normal tissue extracted from 136 H&E histopathology WSIs from the NCT Biobank and the UMM pathology archive, classified into one of nine tissue classes. The training set consists of 100,000 images (referred as NCT-CRC-HE-100K) and the evaluation set consists of 7,180 images (referred as CRC-VAL-HE-7K). Performance was measured using accuracy (Acc.) and balanced accuracy (Bal. Acc.) and results are shown in Table 3.

The Camelyon17-WILDS dataset contains 455,954 im-

Model	Dataset	Patch Size	Tuning	In-domain F1	In-domain AUROC	OOD F1	OOD AUROC
PLUTO	NSCLC	16	Frozen	90.2(1.9)	94.0(1.6)	86.1(2.8)	91.2(2.5)
Meta-DINOv2 ViT-S	NSCLC	14	Frozen	88.6(2.0)	92.0(1.9)	72.1(4.1)	81.9(3.8)
ShuffleNet	NSCLC	-	Frozen	83.6(2.4)	90.1(2.0)	72.2(4.2)	83.5(3.5)
ShuffleNet	NSCLC	-	Fine-tuned	88.1(2.2)	93.9(1.5)	42.5(8.0)	90.8(2.1)
PLUTO	HER2	16	Frozen	71.5(2.8)	89.5(1.5)	71.0(3.0)	93.7(1.1)
Meta-DINOv2 ViT-S	HER2	14	Frozen	56.4(3.2)	83.4(1.7)	57.2(3.5)	88.7(1.3)
ShuffleNet	HER2	-	Frozen	51.3(3.2)	84.4(1.7)	46.6(3.0)	86.5(1.5)
ShuffleNet	HER2	-	Fine-tuned	62.9(3.1)	87.2(1.5)	66.3(3.4)	91.6(1.3)

Table 2. Performance of MIL models with different ViT- and CNN-based featurizers on NSCLC subtyping and HER2 scoring tasks. The mean and standard deviation across 1,000 bootstrapped runs are reported. We note that MIL models that use our frozen PLUTO model as a featurizer tend to outperform models with both frozen and fine-tuned CNN backbones (ShuffleNet), Imagenet-pre-trained ViT backbones, and similar pathology pre-trained ViTs where applicable (NSCLC subtyping). This is especially evident in OOD performance, highlighting the robustness of PLUTO’s embeddings.

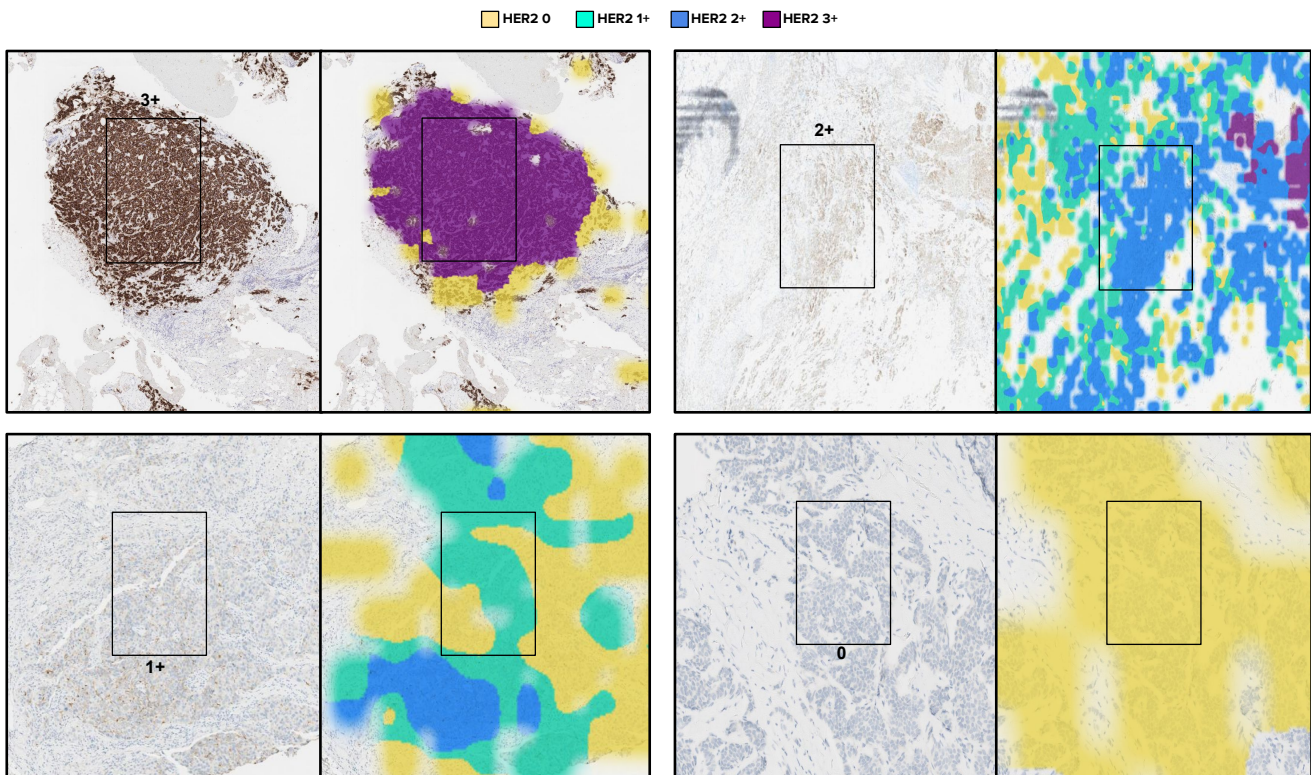


Figure 4. Comparison of AdditiveMIL heatmaps (right) from PLUTO against ground truth ROIs (left) for HER2 scores 3+, 2+, 1+, 0. There is considerable alignment between the ground truth ROIs and the PLUTO model’s region-level predictions, indicating that the model is learning biologically-relevant features when making slide-level predictions.

ages (96×96 pixels at 1 mpp, downsampled from 0.25 mpp slides) from 50 WSIs of breast cancer metastases in lymph node sections from five different hospitals. The task is a binary classification of whether the central 32×32 region contains tumor tissue. The training set consists of 302,436 tiles from 30 WSIs from three hospitals, the ID validation set of 33,560 from the same 30 WSIs, the OOD validation

set of 34,904 from 10 WSIs from the fourth hospital, and the OOD test set of 85,054 from 10 WSIs from the fifth hospital. Each split has a 50/50 class balance. Performance was evaluated using accuracy in the OOD test set, measuring robustness to shifts across hospitals (Table 3).

The results of our embedding probing on these external tissue classification datasets are summarized in Table

Model	Adaptation Head	Benchmark Name	Metrics	
PLUTO ResNet50*	Linear Head N/A	H&E CRC-100K H&E CRC-100K	Acc.	Bal. Acc.
			96.6	95.3
PLUTO DenseNet-121*	Linear Head N/A	Camelyon17-WILDS Camelyon17-WILDS	Acc.	Bal. Acc.
			96.2	-
PLUTO PLUTO UNet*	Mask2Former Mask R-CNN N/A	GlaS GlaS GlaS	DICE	IoU
			91.2	84.5
			88.0	79.6
PLUTO PLUTO ResNet50 + Mask R-CNN* [47]	HoverNet Mask R-CNN N/A	PanNuke PanNuke PanNuke	bPQ	mPQ
			67.1	47.7
			58.6	-
			55.3	36.9

*Fully Supervised Baseline Model

Table 3. Summary of PLUTO performance across public datasets. Details of the tasks associated with the datasets are outlined in Table 1. We perform the tile classification task on CRC-100K and Camelyon17-WILDS datasets by linear probing the PLUTO embeddings while keeping the backbone frozen. PLUTO, while significantly smaller, achieves strong performance and is competitive with the best performing models that have been reported for these two datasets, highlighting the effectiveness of diverse pre-training data for enhancing robustness. We perform the gland segmentation and nuclei segmentation tasks on the GlaS and PanNuke datasets, respectively, by adapting PLUTO through multiple adaptation strategies while keeping the backbone frozen. PLUTO achieves state-of-the-art performance on gland segmentation, outperforming other fully supervised segmentation frameworks. PLUTO beats fine-tuned backbone baselines of comparable size on the PanNuke dataset, and is competitive with significantly larger fine-tuned backbones that have been reported for PanNuke.

3. PLUTO obtained competitive performance in both the CRC-100K dataset and Camelyon17-WILDS dataset with the best performing models that have been reported on these datasets, despite having significantly fewer parameters and a smaller—but highly diverse—pre-training dataset.

4.2.2 Tile Classification: Proprietary Datasets

We probe the CLS-token and patch-token embeddings on tile-level tissue classification in a broad set of indications and stains. All labels are derived from board-certified pathologists, and substances are chosen to capture the most relevant biology in those indications. In particular, we consider the following to test the adaptability of PLUTO across diverse diseases, stains, and organs:

- Four-class H&E Pan-Oncology Tissue: cancer, necrosis, cancer-associated stroma, normal tissue
- Four-class IHC Pan-Oncology Tissue: cancer, necrosis, cancer-associated stroma, normal tissue
- 10-class H&E Inflammatory Bowel Disease (IBD) Tissue: crypt abscess, inter-gland lumen, infiltrated epithelium, normal tissue, other tissue, blood vessel, granulation tissue, erosion or ulceration, lamina propria, muscularis mucosa.

A FlexiViT patch size of 16×16 was used for tissue

tasks, while 8×8 is used for cell classification. We begin by treating the tissue task as a simple tile classification problem and use an MLP on top of the CLS tokens for probing. Along with simple probing, we use a variant of attentive probing [11], where the CLS embedding is augmented by concatenating an attention-pooled summary of the patch-tokens. The attention pooling allows the classifier to learn relevant context from across the entire image, and results in a performance improvement over only using the CLS embedding. Supplementary Tables 12, 13 show macro-F1 scores for each model and embedding pooling set-up.

Comparing Oncology and IBD Tissue results demonstrates that the best adaptation approach is dependent on the target task. On a four-class tissue problem, the CLS token holds the vast majority of the necessary signal, and adding the learned attention pooling results in less significant benefits. However, in 10-class IBD Tissue, the classifier struggles when relying only on the CLS token and must instead learn to attend to selective patches.

To contextualize the results, we train a ResNet-style fully supervised CNN model from scratch on the same dataset. We demonstrate that by using PLUTO in combination with a small amount of labeled data and an optimal adaptation approach, we out-perform the baseline fully-supervised

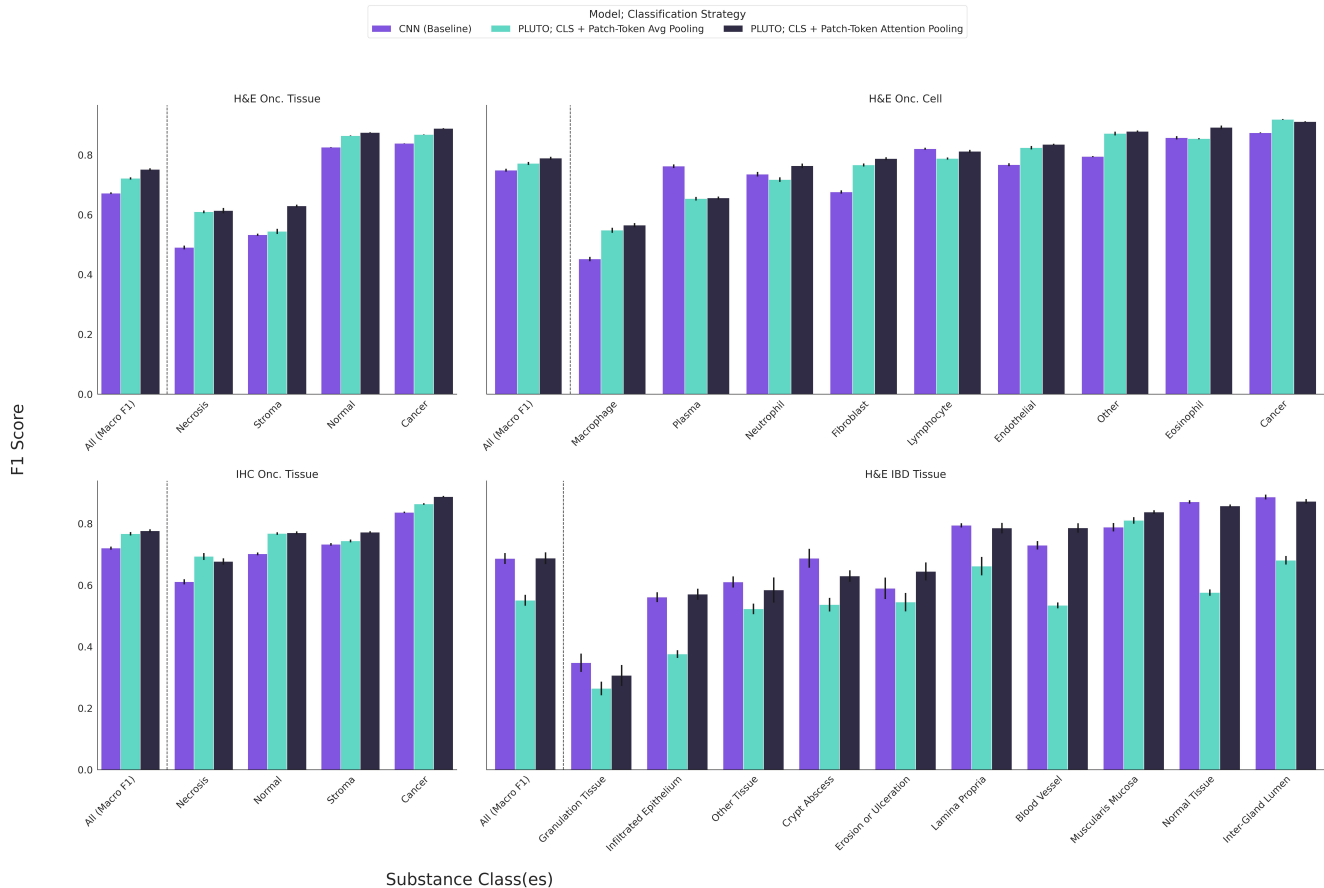


Figure 5. Linear and Attention Probing performance of PLUTO on proprietary tile classification benchmarks at the substance level. For each model, the left-most bar highlights the macro-F1 score on the dataset. PLUTO outperforms a fully supervised CNN baseline. Attentive pooling of patch-tokens provides more flexible adaptation and has the best performance across datasets. For the Oncology cell classification task, patch-token information from the central window is needed to capture context to classify the cell at the center pixel, so average pooling and attention pooling perform comparably. While patch embeddings do contain relevant information for the more complicated task of IBD tissue classification, performance significantly improves on applying attention pooling on top of them.

model on Oncology indications and achieve statistically equivalent performance on IBD Tissue Classification. We reason that the level of detail necessary to distinguish morphology among IBD classes warrants further exploration into optimal light-weight methods for extracting information from frozen embeddings. Figure 5 captures the class-level and aggregated performance for all datasets.

4.2.3 Gland Segmentation: Public Datasets

Gland morphology is used in gastrointestinal (GI) tract pathology. The architectural appearance of glands is vital for cancer grading in colorectal carcinoma [14]. In ulcerative colitis or IBD, changes in crypt architecture (density, morphology, etc.) are a core component of the Geboes scoring system [24]. Outside of the GI tract, gland differentiation is important for diagnosis and grading in breast and other cancers [15]. We evaluated the performance on the

GlaS [48] dataset, which consists of 85 images for training and 80 images for testing for a total of 165 images derived from 16 H&E-stained sections of stage T3 or T42 colorectal adenocarcinoma. These slides were scanned using a Zeiss MIRAX MIDI Slide Scanner with a resolution of 0.465 mpp and varying image sizes (most commonly 775×522). Results are shown in Table 3. Performance was measured using dice coefficient (Dice) and Intersection over Union (IoU) in the test set. To the best of our knowledge, this is the first pathology FM used in a gland segmentation task. Results show state-of-the-art performance, with PLUTO outperforming other fully-supervised segmentation frameworks. This underscores the ability of our proposed approach to successfully adapt to a new tissue-level segmentation task with limited labeled data.

4.2.4 Gland Segmentation: Proprietary Datasets

We also curate an internal instance segmentation dataset to segment glands across stains, organs, and disease areas. We discuss the characteristics of the dataset in Table 10 and results in Figure 6 with qualitative comparisons in Figure 7. We train on samples of size 768×768 at a resolution of 1 mpp using our proposed adaptation approaches using a patch size of 16. Both of our adaptation approaches beat the Mask R-CNN baseline using a frozen ResNet50 backbone, with the Mask2Former adaptation head providing the highest performance across all metrics. We further experiment with a patch size of 32 and notice a very minor performance drop (1%) but significantly higher inference throughput. We notice that Mask2Former works better on glands where the objects are not close to convex-like shapes; we hypothesize that the query based segmentation mechanism is helping the network, and we aim to explore this further in future work.

4.3. Cellular- and Subcellular-level Results

4.3.1 Tile Classification: Proprietary Datasets

Tile classification is extended to a nine-class H&E Oncology cell benchmark: Macrophages, Plasma Cells, Neutrophils, Fibroblasts, Lymphocytes, Endothelial Cells, Eosinophils, Cancer Cells, and Other Cells. The label for each tile is derived from the cell class present at the center pixel of the tile. Because the CLS token does not capture the granular information needed for cell classification, we concatenate it with an average pooling of the four central patch token embeddings. We then extend the approach to Attention Pooling in the same fashion as Section 4.2.2 by allowing the learned attention layer to see all patch tokens in the tile. The result is shown alongside the tissue classification tasks in Figure 5, and full ablations are in Supplementary Tables 12, 13. The context in the center four patch tokens provides sufficient signal for cell classification, but learned attention pooling on the entire tile achieves slightly better results on almost all substances.

4.3.2 Nuclei and Cell Segmentation: Public Datasets

Instance segmentation is a popular approach for nucleus, cytoplasm, and cell quantification on H&E and IHC-stained WSIs [1].

We evaluated the performance of our adaptation strategies on the PanNuke [22] dataset. It consists of 481 visual fields across 19 different tissue types from WSIs from TCGA and a local hospital, with a total of 189,744 exhaustive nuclei labels categorized into five classes. The visual fields were randomly sampled from more than 20,000 WSIs that were scanned at either $40\times$ or $20\times$ and re-sized to $40\times$. Following the original publishers of this dataset, we report binary panoptic quality (bPQ) and multi-class panop-

tic quality (mPQ) in Table 3. For the ablation study comparing different adaptation heads, experiments were conducted in the binary configuration where nuclei were not classified, and therefore only bPQ is reported. The experimental setup used an inference patch size of 16 for the HoverNet architecture due to its design. All conducted experiments were thus performed using this specified patch size.

Results demonstrated that despite its significantly smaller architecture, PLUTO (without fine-tuning) achieved nuclei segmentation performance comparable to state-of-the-art with much larger models that have been reported on this dataset. In the binary setup, the comparison of the HoverNet adaptation head to the Mask R-CNN variation highlighted the advantage of using specialized adaptation architectures designed in favor of nuclei segmentation.

4.3.3 Nuclei and Cell Segmentation: Proprietary Datasets

IHC [40] is a widely used tool in pathology for disease diagnosis and subtyping, cell classification, and quantification of protein abundance. IHC staining utilizes antibodies targeted against certain antigens in specific tissues and cells to directly quantify protein abundance, and often its localization within the cell (e.g., membranous, cytoplasmic, or nuclear staining). Thus, especially in IHC, it is important not only to identify individual cells and nuclei but also to precisely delineate their boundaries. We curate internal datasets for IHC Cell Segmentation, IHC and H&E Nuclei Segmentation. We describe the characteristics of our proprietary nuclei and cell segmentation datasets in Tables 14 and 11 in the Supplementary Section. We compare Mask R-CNN with ResNet50 and ViT backbones using patch size 8, and compare Mask R-CNN with a Mask2Former adaptation head. The results from these experiments on IHC Nuclei and Cell Segmentation and H&E Nuclei Segmentation are summarized in Figure 6 with qualitative comparisons in Figure 7. We train on samples of size 384×384 at a resolution of 0.25 mpp. We find that our adaptation approaches beat the Mask R-CNN baseline using a frozen ResNet50 backbone.

4.4. Deployability

Given the increasing adoption of ML in digital pathology for clinical and diagnostic use-cases, there is a need for ML algorithms which are robust and can be deployed at scale to address patient and clinician needs. Real-world deployment of ML algorithms needs careful consideration of factors like deployment throughput, algorithm latency for end-users, and cost of deployment. While FMs can enable new capabilities and improve generalization, they are often orders of magnitude larger than task-specific models, and deploying them on WSIs can be significantly more expensive

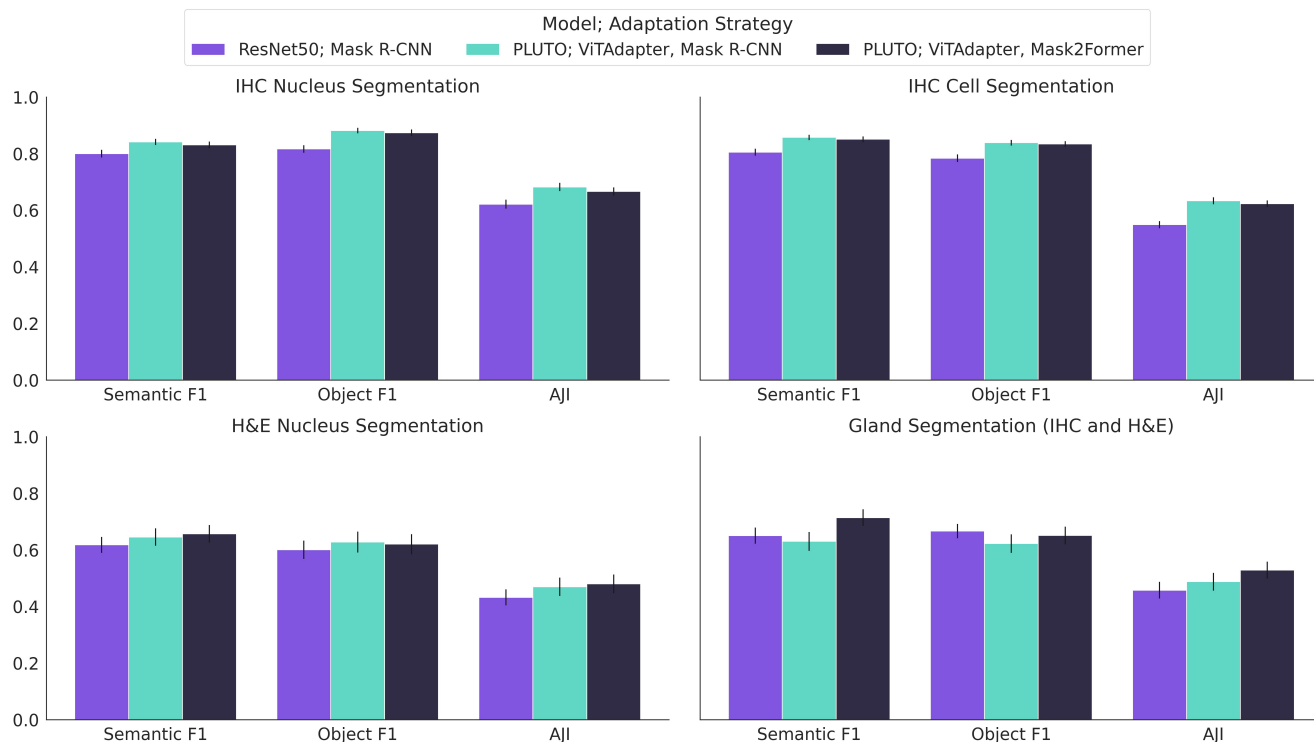


Figure 6. Instance segmentation performance on our proprietary datasets across IHC nuclei segmentation, IHC cell segmentation, H&E nuclei segmentation, and gland segmentation (H&E and IHC). Point estimates show the average metric across the set of tiles, and error bars represent a 95% confidence interval. The baseline performance is established with a fully supervised Mask R-CNN model with a ResNet50 backbone. The PLUTO ViTAdapter + Mask R-CNN and ViTAdapter + Mask2Former adaptation heads are fine-tuned while the backbone is kept frozen. We note that our flexible patch size approach allowed us to change the patch size across tasks while leaving the PLUTO weights frozen.

and time-consuming.

To develop a backbone which is performant and robust while being suitable for deployment at scale, we make two key design choices for PLUTO. We choose the ViT architecture ViT-S as our backbone, as it is light-weight while still having enough model capacity to be performant at different tasks. Additionally, the FlexiViT architecture enables customization of the patch size, which not only enables selecting the optimal patch size for a downstream task, but can also be used to improve model throughput as the patch size controls the sequence length. To illustrate the efficiency of PLUTO, we compare the throughput efficiency of various ViT backbones (ViT-S, ViTB, ViT-L, ViT-H) for two common pathology tasks: tile classification and slide-level prediction. We fix the task-specific adaptation heads—linear layer for patch-classification, and AdditiveMIL for slide-level prediction—while varying the backbone, and measure the throughput in tiles/second with a tile size of 224×224 and a patch size of 16. We note that we have not applied any inference-specific optimizations in this setup. We use the same data-loading pipeline and hardware (A40 GPU) for all the backbones. As seen in Figure 8, for both the

tasks, ViT-S is around $2.5\times$ faster than ViT-B, $7.5\times$ faster than ViT-L, and $15\times$ faster than ViT-H.

5. Summary and Future Work

We present in this paper PLUTO: a competitive state-of-the-art pathology Foundation Model based on a light-weight ViT that is pre-trained on a diverse dataset from over 50 distinct sites consisting of over 195 million unique image tiles across four resolutions (0.25, 0.5, 1, and 2 mpp) sampled from 158, 852 WSIs, over 16 tissue groups, and 28 disease areas. We implement the PLUTO pre-training scheme by modifying the DINOv2 [44] self-supervised training strategy to incorporate different patch sizes and WSI tile resolutions through extending the FlexiViT [4] framework. We further modify the DINOv2 loss function by adding a MAE [28] objective term and introducing a Fourier loss term that encourages capturing low-frequency and high-frequency features.

PLUTO is designed to take advantage of the multi-scale nature of WSIs and provide informative representations across biological scales. We have quantified the perfor-

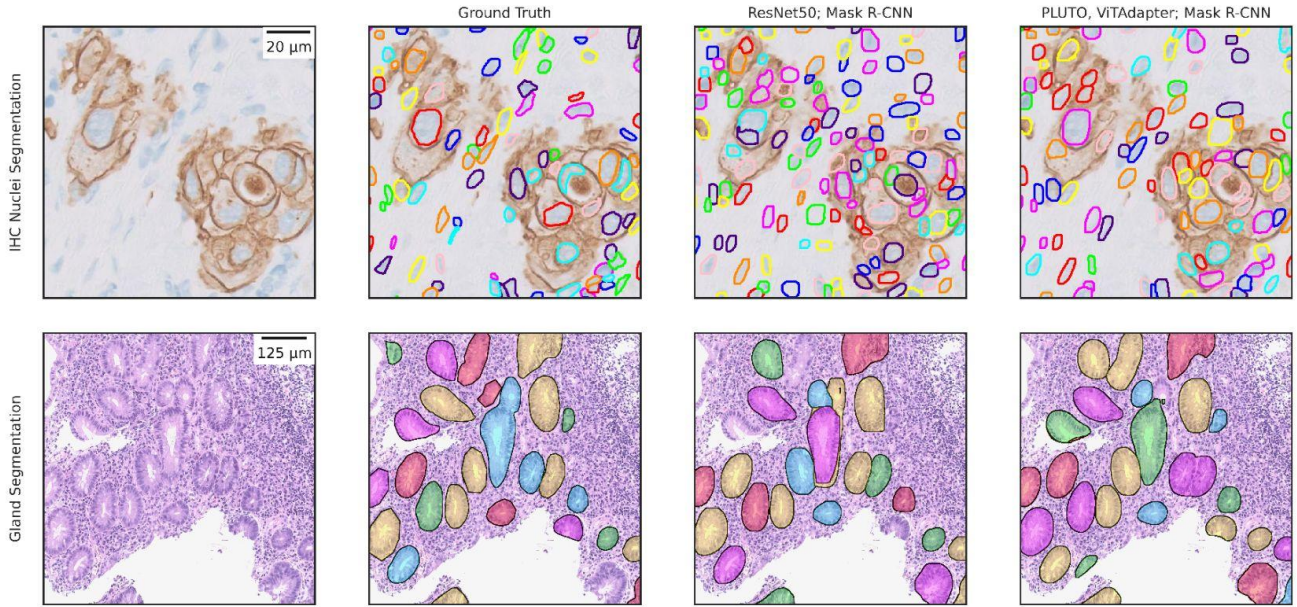


Figure 7. Comparison of instance segmentation masks across models at the subcellular level on an IHC slide (top row, Nuclei Segmentation) and at the tissue level on an H&E slide (bottom row, Gland Segmentation) on proprietary datasets. These tiles visualize a representative, smaller field of view within larger labeled tiles where the quantitative performance, characterized here by AJI [36], aligns with dataset-level metrics. IHC Nuclei Segmentation in the whole tile using **ResNet50; Mask R-CNN** reaches 0.448 AJI and using **PLUTO, ViTAdapter; Mask R-CNN** reaches 0.527 AJI. Gland Segmentation on the whole tile using **ResNet50; Mask R-CNN** reaches 0.445 AJI and using **PLUTO, ViTAdapter; Mask R-CNN** reaches 0.450 AJI. In both cases, PLUTO outperforms the **ResNet50; Mask R-CNN** baseline.

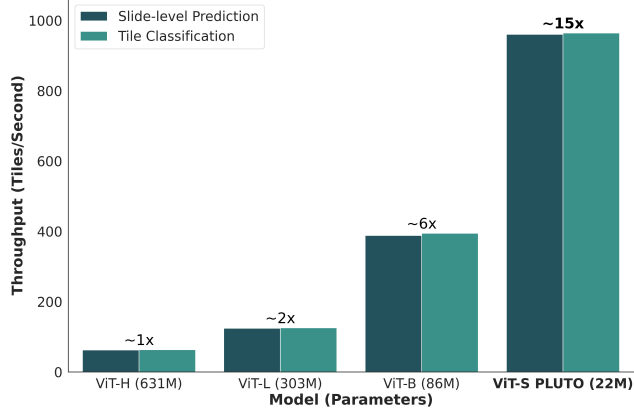


Figure 8. Throughput (tiles/sec) of models for tile-level and slide-level classification tasks with various backbones using patch size 16 with a tile size 224×224 . We use linear probes and AdditiveMIL classifiers as adaptation heads respectively for the tile and slide-level classification tasks. Notable pathology FMs use ViT-H [54], ViT-L [10] [18] and ViT-B [21].

performance of our self-supervised backbone on a variety of adaptation tasks across biological scales, namely:

- **Slide-level classification** We adapt PLUTO to slide-level scoring tasks with multiple instance learning (MIL) and

achieve superior OOD performance on NSCLC subtyping and HER2 scoring.

- **Tile Classification: Tissue** We adapt PLUTO to a nine-class tissue classification task on the NCT-CRC dataset [34] and to a binary breast cancer classification task on the Camelyon17-WILDS [35] dataset. We demonstrate results competitive with state-of-the-art methods that have been reported on these two datasets. We additionally quantify the quality of these representations (Section 4.2.2) on a variety of tasks on multiple proprietary datasets, namely on a four-class tissue classification task across oncology indications on H&E and IHC-stained WSIs, and on a 10-class tissue classification task for IBD. PLUTO matches or outperforms a supervised CNN baseline in these datasets.
- **Instance Segmentation: Gland Segmentation** We adapt PLUTO with Mask R-CNN and Mask2Former adaptation heads respectively to identify glands through instance segmentation. We quantify the performance of this approach with two datasets: the public GlaS [48] dataset and our proprietary gland annotations. On the GlaS dataset, we achieve state-of-the-art performance compared to public strongly-supervised benchmarks. On our internal dataset, PLUTO performs superior to ResNet50 backbone using our Mask2Former approach.
- **Tile Classification: Cells and Nuclei** We quantify the

quality of PLUTO embeddings on a tile classification task of nine-class cell classification across H&E stained slides, where we also outperform a supervised CNN baseline.

- **Instance Segmentation: Cells and Nuclei** We adapt PLUTO with Mask R-CNN and Mask2Former adaptation heads respectively to identify cells and nuclei through instance segmentation. We have measured the performance of this approach with four segmentation datasets – one public (PanNuke [22]) and three proprietary. We achieve a higher performance with our PLUTO Mask R-CNN and Mask2Former adaptation heads on our proprietary datasets than baselines we have established with a ResNet50 backbone. We additionally adapt PLUTO with the HoverNet architecture [23] to identify nuclei on the PanNuke dataset, where we achieve performance competitive to state-of-the-art methods that have been reported on PanNuke.

Our work also demonstrates the importance of data diversity, along with the incorporation of biological priors in the construction of pre-training datasets and the design of the model architecture for large-scale self-supervised models. PLUTO was trained with the ViT-S architecture consisting of 22 million parameters, which is significantly fewer than the number of parameters of the other pathology FMs discussed in Section 1. Despite its smaller size, we demonstrate competitive OOD performance on public benchmarks spanning tile classification, WSI-level prediction, and instance segmentation. Additionally, the smaller model size of PLUTO and the flexibility to customize the patch size enables a significantly faster inference time in comparison to other pathology FMs, which makes PLUTO well-suited for deployments at scale. Our results hint that dataset diversity could be an additional empirical scaling law that complements the well-established scaling laws of dataset size, model size and amount of compute [33]. Further research is needed, however, to establish empirical scaling laws for digital pathology in order to understand the impact of dataset diversity, dataset size, model size, and amount of compute on model performance, robustness, and deployability.

A multi-scale pathology FM that learns strong representations across biological scales and demonstrates robust performance on tasks across these scales will enable computational pathology to shift from bespoke single-task models towards more general AI models that can address long-standing problems with diverse applications in pathology. We hope that our efforts with PLUTO further motivate building high-performing, deployable FMs; drive FM adoption in pathology; and serve real-world translational research and clinical applications.

References

[1] John Abel, Suyog Jain, Deepta Rajan, Harshith Padigela, Kenneth Leidal, Aaditya Prakash, Jake Conway, Michael

Nercessian, Christian Kirkup, Syed Ashar Javed, Raymond Biju, Natalia Harguindeguy, Daniel Shenker, Nicholas Indorf, Darpan Sanghavi, Robert Egger, Benjamin Trotter, Ylaine Gerardin, Jacqueline A. Brosnan-Cashman, Aditya Dhoot, Michael C. Montalto, Chintan Parmar, Ilan Wapinski, Archit Khosla, Michael G. Drage, Limin Yu, and Amaro Taylor-Weiner. Deep-learning quantified cell-type-specific nuclear morphology predicts genomic instability and prognosis in multiple cancer types. *bioRxiv*, 2024. 13

[2] Peter Bandi, Oscar Geessink, Quirine Manson, Marcory Van Dijk, Maschenka Balkenhol, Meyke Hermsen, Babak Ehteshami Bejnordi, Byungjae Lee, Kyunghyun Paeng, Aoxiao Zhong, Quanzheng Li, Farhad Ghazvinian Zanjani, Svitlana Zinger, Keisuke Fukuta, Daisuke Komura, Vlado Ovtcharov, Shenghua Cheng, Shaoqun Zeng, Jeppe Thagaard, Anders B Dahl, Huangjing Lin, Hao Chen, Ludwig Jacobsson, Martin Hedlund, Melih Cetin, Eren Halici, Hunter Jackson, Richard Chen, Fabian Both, Jorg Franke, Heidi Kusters-Vandeveld, Willem Vreuls, Peter Bult, Bram van Ginneken, Jeroen van der Laak, and Geert Litjens. From Detection of Individual Metastases to Classification of Lymph Node Status at the Patient Level: The CAMELYON17 Challenge. *IEEE Transactions on Medical Imaging*, 38:550–560, 2019. 9

[3] Reda Bensaid, Vincent Gripon, François Leduc-Primeau, Lukas Mauch, Ghouthi Boukli Hacene, and Fabien Cordinaux. A Novel Benchmark for Few-Shot Semantic Segmentation in the Era of Foundation Models. *arXiv:2401.11311*, 2024. 2

[4] Lucas Beyer, Pavel Izmailov, Alexander Kolesnikov, Mathilde Caron, Simon Kornblith, Xiaohua Zhai, Matthias Minderer, Michael Tschannen, Ibrahim Alabdulmohsin, and Filip Pavetic. FlexiViT: One Model for All Patch Sizes. In *2023 IEEE/CVF Conference on Computer Vision and Pattern Recognition (CVPR)*, pages 14496–14506, Los Alamitos, CA, USA, 2023. IEEE Computer Society. 4, 6, 14

[5] Jaime Bosch, Chuhan Chung, Oscar M Carrasco-Zevallos, Stephen A Harrison, Manal F Abdelmalek, Mitchell L Shiffman, Don C Rockey, Zahil Shanis, Dinkar Juyal, Harsha Pokkalla, et al. A Machine Learning Approach to Liver Histological Evaluation Predicts Clinically Significant Portal Hypertension in NASH Cirrhosis. *Hepatology*, 74(6):3146–3160, 2021. 2

[6] Wouter Bulten, Hans Pinckaers, Hester van Boven, Robert Vink, Thomas de Bel, Bram van Ginneken, Jeroen van der Laak, Christina Hulsbergen-van de Kaa, and Geert Litjens. Automated deep-learning system for Gleason grading of prostate cancer using biopsies: a diagnostic study. *The Lancet Oncology*, 21(2):233–241, 2020.

[7] Gabriele Campanella, Matthew G Hanna, Luke Geneslaw, Allen Mirafior, Vitor Werneck Krauss Silva, Klaus J Busam, Edi Brogi, Victor E Reuter, David S Klimstra, and Thomas J Fuchs. Clinical-grade computational pathology using weakly supervised deep learning on whole slide images. *Nature medicine*, 25(8):1301–1309, 2019. 2

[8] Mathilde Caron, Hugo Touvron, Ishan Misra, Hervé Jégou, Julien Mairal, Piotr Bojanowski, and Armand Joulin. Emerging Properties in Self-Supervised Vision Transformers, 2021. 2, 6

- [9] Richard J. Chen, Chengkuan Chen, Yicong Li, Tiffany Y. Chen, Andrew D. Trister, Rahul G. Krishnan, and Faisal Mahmood. Scaling Vision Transformers to Gigapixel Images via Hierarchical Self-Supervised Learning. In *Proceedings of the IEEE/CVF Conference on Computer Vision and Pattern Recognition (CVPR)*, pages 16144–16155, 2022. [2](#)
- [10] Richard J Chen, Tong Ding, Ming Y Lu, Drew FK Williamson, Guillaume Jaume, Bowen Chen, Andrew Zhang, Daniel Shao, Andrew H Song, Muhammad Shaban, et al. Towards a General-Purpose Foundation Model for Computational Pathology. *Nature Medicine*, 2024. [2](#), [15](#), [21](#)
- [11] Xiaokang Chen, Mingyu Ding, Xiaodi Wang, Ying Xin, Shentong Mo, Yunhao Wang, Shumin Han, Ping Luo, Gang Zeng, and Jingdong Wang. Context Autoencoder for Self-Supervised Representation Learning, 2023. [11](#)
- [12] Zhe Chen, Yuchen Duan, Wenhai Wang, Junjun He, Tong Lu, Jifeng Dai, and Yu Qiao. Vision Transformer Adapter for Dense Predictions. *arXiv preprint arXiv:2205.08534*, 2022. [8](#)
- [13] Bowen Cheng, Alexander G. Schwing, and Alexander Kirillov. Per-Pixel Classification is Not All You Need for Semantic Segmentation. 2021. [8](#)
- [14] Carolyn C Compton. Updated protocol for the examination of specimens from patients with carcinomas of the colon and rectum, excluding carcinoid tumors, lymphomas, sarcomas, and tumors of the vermiform appendix: a basis for checklists. *Archives of pathology & laboratory medicine*, 124(7):1016–1025, 2000. [12](#)
- [15] Gábor Cserni and Anita Sejbén. Grading ductal carcinoma in situ (DCIS) of the breast—what’s wrong with it? *Pathology & Oncology Research*, 26(2):665–671, 2020. [12](#)
- [16] James A. Diao, Jason K. Wang, Wan Fung Chui, Victoria Mountain, Sai Chowdary Gullapally, Ramprakash Srinivasan, Richard N. Mitchell, Benjamin Glass, Sara Hoffman, Sudha K. Rao, Chirag Maheshwari, Abhik Lahiri, Aaditya Prakash, Ryan McLoughlin, Jennifer K. Kerner, Murray B. Resnick, Michael C. Montalto, Aditya Khosla, Ilan N. Wapinski, Andrew H. Beck, Hunter L. Elliott, and Amaro Taylor-Weiner. Human-interpretable image features derived from densely mapped cancer pathology slides predict diverse molecular phenotypes. *Nature Communications*, 12(1), 2021. [2](#)
- [17] James A Diao, Jason K Wang, Wan Fung Chui, Victoria Mountain, Sai Chowdary Gullapally, Ramprakash Srinivasan, Richard N Mitchell, Benjamin Glass, Sara Hoffman, Sudha K Rao, et al. Human-interpretable image features derived from densely mapped cancer pathology slides predict diverse molecular phenotypes. *Nature communications*, 12(1):1–15, 2021. [2](#)
- [18] Jonas Dippel, Barbara Feulner, Tobias Winterhoff, Simon Schallenberg, Andreas Kunft Gabriel Dernbach, Stephan Tietz, Timo Milbich, Simon Heinke, Marie-Lisa Eich, Julika Ribbat-Idel, Rosemarie Krupar, Philipp Jurmeister, David Horst, Lukas Ruff, Klaus-Robert Müller, Frederick Klauschen, and Maximilian Alber. RudolfV: A Foundation Model by Pathologists for Pathologists, 2024. [2](#), [15](#), [21](#)
- [19] Alexey Dosovitskiy, Lucas Beyer, Alexander Kolesnikov, Dirk Weissenborn, Xiaohua Zhai, Thomas Unterthiner, Mostafa Dehghani, Matthias Minderer, Georg Heigold, Sylvain Gelly, Jakob Uszkoreit, and Neil Houlsby. An Image is Worth 16x16 Words: Transformers for Image Recognition at Scale, 2021. [2](#)
- [20] Babak Ehteshami Bejnordi, Mitko Veta, Paul Johannes van Diest, Bram van Ginneken, Nico Karssemeijer, Geert Litjens, Jeroen A. W. M. van der Laak, , and the CAMELYON16 Consortium. Diagnostic Assessment of Deep Learning Algorithms for Detection of Lymph Node Metastases in Women With Breast Cancer. *JAMA*, 318(22):2199–2210, 2017. [1](#)
- [21] Alexandre Filiot, Ridouane Ghermi, Antoine Olivier, Paul Jacob, Lucas Fidon, Alice Mac Kain, Charlie Saillard, and Jean-Baptiste Schiratti. Scaling Self-Supervised Learning for Histopathology with Masked Image Modeling. *medRxiv*, 2023. [2](#), [15](#), [21](#)
- [22] Jevgenij Gamper, Navid Alemi Koohbanani, Ksenija Benet, Ali Khuram, and Nasir Rajpoot. PanNuke: an open pancreatic histology dataset for nuclei instance segmentation and classification. In *European Congress on Digital Pathology*, pages 11–19. Springer, 2019. [9](#), [13](#), [16](#)
- [23] Simon Graham, Quoc Dang Vu, Shan E Ahmed Raza, Ayesha Azam, Yee Wah Tsang, Jin Tae Kwak, and Nasir Rajpoot. Hover-net: Simultaneous segmentation and classification of nuclei in multi-tissue histology images. *Medical Image Analysis*, page 101563, 2019. [16](#)
- [24] Simon Graham, Fayyaz Minhas, Mohsin Bilal, Mahmoud Ali, Yee Wah Tsang, Mark Eastwood, Noorul Wahab, Mostafa Jahanifar, Emily Hero, Katherine Dodd, et al. Screening of normal endoscopic large bowel biopsies with artificial intelligence: a retrospective study. *medRxiv*, pages 2022–10, 2022. [12](#)
- [25] Sai Chowdary Gullapally, Yibo Zhang, Nitin Kumar Mittal, Deeksha Kartik, Sandhya Srinivasan, Kevin Rose, Daniel Shenker, Dinkar Juyal, Harshith Padigela, Raymond Biju, Victor Minden, Chirag Maheshwari, Marc Thibault, Zvi Goldstein, Luke Novak, Nidhi Chandra, Justin Lee, Aaditya Prakash, Chintan Shah, John Abel, Darren Fahy, Amaro Taylor-Weiner, and Anand Sampat. Synthetic Domain-Targeted Augmentation (S-DOTA) Improves Model Generalization in Digital Pathology, 2023. [2](#)
- [26] Hasan Abed Al Kader Hammoud, Tuhin Das, Fabio Pizzati, Philip Torr, Adel Bibi, and Bernard Ghanem. On pretraining data diversity for self-supervised learning, 2024. [2](#)
- [27] Kaiming He, Georgia Gkioxari, Piotr Dollár, and Ross Girshick. Mask R-CNN. In *2017 IEEE International Conference on Computer Vision (ICCV)*, pages 2980–2988, 2017. [8](#)
- [28] Kaiming He, Xinlei Chen, Saining Xie, Yanghao Li, Piotr Dollár, and Ross Girshick. Masked autoencoders are scalable vision learners. In *Proceedings of the IEEE/CVF Conference on Computer Vision and Pattern Recognition (CVPR)*, pages 16000–16009, 2022. [4](#), [6](#), [14](#), [21](#)
- [29] Mahdi Hosseini, Babak Ehteshami Bejnordi, Vincent Quoc-Huy Trinh, Lyndon Chan, Danial Hasan, Xingwen Li,

- Stephen Yang, Taehyo Kim, Haochen Zhang, Theodore Wu, Kajanan Chinniah, Sina Maghsoudlou, Ryan Zhang, Jiadai Zhu, Samir Khaki, Andrei Buin, Fatemeh Chaji, Ala Salehi, Bich Nguyen, and Konstantinos Plataniotis. Computational Pathology: A Survey Review and The Way Forward. *Journal of Pathology Informatics*, 15:100357, 2024. 2
- [30] Maximilian Ilse, Jakub Tomczak, and Max Welling. Attention-based deep multiple instance learning. In *International conference on machine learning*, pages 2127–2136. PMLR, 2018. 7
- [31] Syed Ashar Javed, Dinkar Juyal, Harshith Padigela, Amaro Taylor-Weiner, Limin Yu, and Aaditya Prakash. Additive MIL: Intrinsically Interpretable Multiple Instance Learning for Pathology. In *Advances in Neural Information Processing Systems*, 2022. 2, 7, 9
- [32] Mingu Kang, Heon Song, Seonwook Park, Donggeun Yoo, and Sérgio Pereira. Benchmarking Self-Supervised Learning on Diverse Pathology Datasets. In *Proceedings of the IEEE/CVF Conference on Computer Vision and Pattern Recognition (CVPR)*, pages 3344–3354, 2023. 2, 21
- [33] Jared Kaplan, Sam McCandlish, Tom Henighan, Tom B. Brown, Benjamin Chess, Rewon Child, Scott Gray, Alec Radford, Jeffrey Wu, and Dario Amodei. Scaling laws for neural language models, 2020. 16
- [34] Jakob Nikolas Kather, Niels Halama, and Alexander Marx. 100,000 histological images of human colorectal cancer and healthy tissue, 2018. 9, 15
- [35] Pang Wei Koh, Shiori Sagawa, Henrik Marklund, Sang Michael Xie, Marvin Zhang, Akshay Balsubramani, Weihua Hu, Michihiro Yasunaga, Richard Lanus Phillips, Irena Gao, Tony Lee, Etienne David, Ian Stavness, Wei Guo, Berton A. Earnshaw, Imran S. Haque, Sara Beery, Jure Leskovec, Anshul Kundaje, Emma Pierson, Sergey Levine, Chelsea Finn, and Percy Liang. WILDS: A Benchmark of in-the-Wild Distribution Shifts. *International Conference on Machine Learning*, 2021. 9, 15
- [36] Neeraj Kumar, Ruchika Verma, Sanuj Sharma, Surabhi Bhargava, Abhishek Vahadane, and Amit Sethi. A dataset and a technique for generalized nuclear segmentation for computational pathology. *IEEE Transactions on Medical Imaging*, 36(7):1550–1560, 2017. 8, 15, 21
- [37] Jin Li, Deepta Rajan, Chintan Shah, Dinkar Juyal, Shreya Chakraborty, Chandan Akiti, Filip Kos, Janani Iyer, Anand Sampat, and Ali Behrooz. Self-training of machine learning models for liver histopathology: Generalization under clinical shifts, 2022. 2
- [38] Ningning Ma, Xiangyu Zhang, Hai-Tao Zheng, and Jian Sun. ShuffleNet V2: Practical Guidelines for Efficient CNN Architecture Design, 2018. 9
- [39] Anant Madabhushi and George Lee. Image analysis and machine learning in digital pathology: Challenges and opportunities. *Medical Image Analysis*, 33:170–175, 2016. 20th anniversary of the Medical Image Analysis journal (MedIA). 1
- [40] Shino Magaki, Seyed A Hojat, Bowen Wei, Alexandra So, and William H Yong. An introduction to the performance of immunohistochemistry. *Methods Mol. Biol.*, 1897:289–298, 2019. 4, 13
- [41] Jesper Molin, Anna Bodén, Darren Treanor, Morten Fjeld, and Claes Lundström. virchow Stain: Multi-Resolution Feature Enhancement in Pathology Visualization. *preprint arXiv:1610.04141*, 2016. 4
- [42] Tan H. Nguyen, Dinkar Juyal, Jin Li, Aaditya Prakash, Shima Nofallah, Chintan Shah, Sai Chowdary Gullapally, Limin Yu, Michael Griffin, Anand Sampat, John Abel, Justin Lee, and Amaro Taylor-Weiner. ContriMix: Scalable stain color augmentation for domain generalization without domain labels in digital pathology, 2024. 2
- [43] OpenAI. GPT-4 Technical Report, 2023. 2
- [44] Maxime Oquab, Timothée Darcet, Theo Moutakanni, Huy V. Vo, Marc Szafraniec, Vasil Khalidov, Pierre Fernandez, Daniel Haziza, Francisco Massa, Alaaeldin El-Nouby, Russell Howes, Po-Yao Huang, Hu Xu, Vasu Sharma, Shangwen Li, Wojciech Galuba, Mike Rabbat, Mido Assran, Nicolas Ballas, Gabriel Synnaeve, Ishan Misra, Herve Jegou, Julien Mairal, Patrick Labatut, Armand Joulin, and Piotr Bojanowski. DINOv2: Learning Robust Visual Features without Supervision, 2023. 2, 6, 9, 14
- [45] PathAI. PathAI Announces Launch of Artifact-Detect Model on AISight, Pioneering Automated Slide Quality Analysis in Pathology Labs, 2023. <https://www.pathai.com/resources/pathai-launches-artifactdetect-model-on-aisight-pioneering-automated-slide-quality-analysis-in-pathology-labs/>. 6
- [46] Tiffany L Sellaro, Robert Filkins, Chelsea Hoffman, Jeffrey L Fine, Jon Ho, Anil V Parwani, Liron Pantanowitz, and Michael Montalto. Relationship between Magnification and Resolution in Digital Pathology Systems. *J. Pathol. Inform*, 2013. 4
- [47] Zhongyi Shui, Yunlong Zhang, Kai Yao, Chenglu Zhu, Yuxuan Sun, and Lin Yang. Unleashing the Power of Prompt-driven Nucleus Instance Segmentation. *arXiv preprint arXiv:2311.15939*, 2023. 11
- [48] Korsuk Sirinukunwattana, Josien P.W. Pluim, Hao Chen, Xiaojuan Qi, Pheng-Ann Heng, Yun Bo Guo, Li Yang Wang, Bogdan J. Matuszewski, Elia Bruni, Urko Sanchez, Anton Böhm, Olaf Ronneberger, Bassem Ben Cheikh, Daniel Racoceanu, Philipp Kainz, Michael Pfeiffer, Martin Urschler, David R.J. Snead, and Nasir M. Rajpoot. Gland segmentation in colon histology images: The glas challenge contest. *Medical Image Analysis*, 35:489–502, 2017. 9, 12, 15
- [49] David Tellez, Geert Litjens, Péter Bánci, Wouter Bulten, John-Melle Bokhorst, Francesco Ciompi, and Jeroen van der Laak. Quantifying the effects of data augmentation and stain color normalization in convolutional neural networks for computational pathology. *Medical Image Analysis*, 58:101544, 2019. 2
- [50] Rishi Bommasani *et al.* On the opportunities and risks of foundation models. *ArXiv*, 2021. 2
- [51] The Cancer Genome Atlas Research Network, John N Weinstein, Eric A Collisson, Gordon B Mills, Kenna R Mills Shaw, Brad A Ozenberger, Kyle Ellrott, Ilya Shmulevich, Chris Sander, and Joshua M Stuart. The cancer genome atlas pan-cancer analysis project. *Nat Genet*, 45(10):1113–1120, 2013. 2, 9

- [52] Hamid Reza Tizhoosh and Liron Pantanowitz. Artificial Intelligence and Digital Pathology: Challenges and Opportunities. *Journal of Pathology Informatics*, 9:38, 2018. [2](#)
- [53] Konstantinos Venetis, Eleonora Crimini, Ehsan Sajjadi, et al. HER2 Low, Ultra-low, and Novel Complementary Biomarkers: Expanding the Spectrum of HER2 Positivity in Breast Cancer. *Frontiers in Molecular Biosciences*, 9:834651, 2022. [9](#)
- [54] Eugene Vorontsov, Alican Bozkurt, Adam Casson, George Shaikovski, Michal Zelechowski, Siqi Liu, Kristen Severson, Eric Zimmermann, James Hall, Neil Tenenholtz, Nicolo Fusi, Philippe Mathieu, Alexander van Eck, Donghun Lee, Julian Viret, Eric Robert, Yi Kan Wang, Jeremy D. Kunz, Matthew C. H. Lee, Jan Bernhard, Ran A. Godrich, Gerard Oakley, Ewan Millar, Matthew Hanna, Juan Retamero, William A. Moye, Razik Yousfi, Christopher Kanan, David Klimstra, Brandon Rothrock, and Thomas J. Fuchs. Virchow: A Million-Slide Digital Pathology Foundation Model, 2023. [2](#), [15](#), [21](#)
- [55] Eric E Walk. The role of pathologists in the era of personalized medicine. *Archives of pathology & laboratory medicine*, 133(4):605–610, 2009. [1](#)
- [56] Dayong Wang, Aditya Khosla, Rishab Gargeya, Humayun Irshad, and Andrew H Beck. Deep learning for identifying metastatic breast cancer. *arXiv preprint arXiv:1606.05718*, 2016. [2](#)
- [57] Wenxuan Wang, Jing Wang, Chen Chen, Jianbo Jiao, Lichao Sun, Yuanxiu Cai, Shanshan Song, and Jiangyun Li. FreMIM: Fourier Transform Meets Masked Image Modeling for Medical Image Segmentation. 2023. [7](#)
- [58] Jinghao Zhou, Chen Wei, Huiyu Wang, Wei Shen, Cihang Xie, Alan Yuille, and Tao Kong. iBOT: Image BERT Pre-Training with Online Tokenizer, 2021. [2](#), [6](#)

PLUTO: Pathology-Universal Transformer

Supplementary Material

Organ	Number of Slides
Breast	19,936
Lower GI	19,185
Lung	15,418
Urinary System	14,167
Skin	13,463
Prostate	12,955
Liver and Biliary Tract	12,840
Lymphatic System	9,586
Female Genital Tract	9,297
Upper GI	7,643
Unknown / Other	6,140
Pancreas	5,097
Head and Neck	5,030
Brain	3,884
Bone and Connective Tissue	2,297
Endocrine	1,547
Male Genital Tract	367

Table 4. Organ distribution of pre-training dataset.

Scanner	Number of Slides
Aperio GT 450	45,476
Aperio AT2	43,905
Aperio NOS	30,107
Philips UFS	12,317
Ventana DP 200	11,686
Unknown / Other	11,272
Hamamatsu S360 C13220	2,318
Hamamatsu XR C12000	1,144
3D Histech Panoramic Scan II	243
Hamamatsu S210 C13239	143
Aperio AT Turbo	138
Hamamatsu 2.0-HT	103

Table 5. Scanner distribution of pre-training dataset.

Objective Magnification	Number of Slides
20×	35,563
40×	123,289

Table 6. Objective magnification distribution of pre-training dataset.

Disease	Number of Slides
Breast Cancer	20,062
Lung Cancer	15,905
Prostate Cancer	13,122
Non-neoplastic Lower GI	12,699
Lymphoma	8,482
Non-neoplastic Liver	8,317
Other Skin Lesion	7,149
Malignant NOS / Other	6,539
Urothelial Cancer	6,477
Unknown / Other	5,753
Gastric Cancer	5,580
Pancreatic Cancer	5,144
Melanoma	4,959
Head and Neck Cancer	4,746
Renal Cell Cancer	4,658
Endometrial Cancer	4,621
Colorectal Cancer	4,134
Glioma	3,562
Ovarian Cancer	3,159
Hepatobiliary Cancer	2,562
Non-neoplastic Other	2,514
Non-neoplastic Upper GI	1,973
Non-neoplastic Kidney	1,587
Cervical Cancer	1,265
Thyroid Cancer	1,023
Sarcoma	979
Basal Cell Cancer	755
Bladder Cancer	684
Multiple Myeloma	442

Table 7. Disease distribution of pre-training dataset.

Stain	Number of Slides
H&E (FFPE)	89,829
IHC	53,498
H&E (Frozen)	7,091
Special Stain	4,856
Unknown / Other	3,578

Table 8. Stain distribution of pre-training dataset. Special stains include trichrome, iron, periodic acid-Schiff, sirius red, Alcian blue, and Grocott-Gomori methenamine silver.

Model	Data Source	Dataset Size	Backbone	Model Size	Method
Virchow [54]	Proprietary (MSKCC)	1.5M WSIs / 2B tiles	ViT-H	632M	DINOv2
UNI [10]	Proprietary (Mass-100K)	100K WSIs / 100M tiles	ViT-L	307M	DINOv2
RudolfV [18]	TCGA + Proprietary	103K WSIs / 750M tiles	ViT-L	307M	DINOv2
Phikon [21]	TCGA	6K WSIs / 43M tiles	ViT-B	86M	iBOT
Kang <i>et al.</i> [32]	TCGA + Proprietary	37K WSIs / 33M tiles	ViT-S	22M	DINOv1
PLUTO (this work)	TCGA + Proprietary (PathAI)	158K WSIs / 195M tiles	FlexiViT-S	22M	Modified DINOv2

Table 9. Survey of recent pathology foundation models. Our proprietary dataset consists of a diverse spectrum of histology stains, scanners, biological objects, and tissue regions across resolution scales sourced from over 50 sites. We customized the DINOv2 training procedure by including a Masked Autoencoder (MAE) [28] loss term, as well a Fourier loss term that decomposes the WSI tile to low- and high-frequency components.

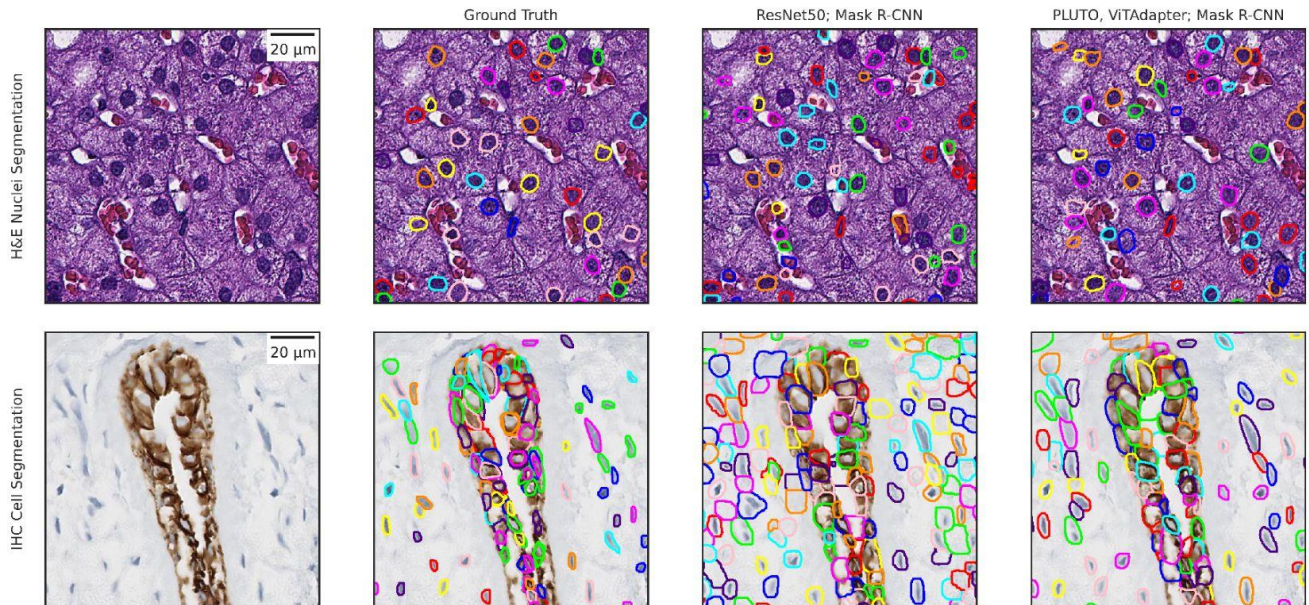


Figure 9. Comparison of segmentation masks across models at the subcellular level on an H&E slide (top row, Nuclei Segmentation) and at the cellular level on an IHC slide (bottom row, Cell Segmentation) on proprietary datasets. These tiles visualize a representative, smaller field of view within larger labeled tiles where the quantitative performance, characterized here by AJI [36], aligns with dataset-level metrics. H&E Nuclei Segmentation in the whole tile using **ResNet50; Mask R-CNN** reaches 0.474 AJI and using **PLUTO, ViTAdapter; Mask R-CNN** reaches 0.585 AJI. IHC Cell Segmentation on the whole tile using **ResNet50; Mask R-CNN** reaches 0.203 AJI and using **PLUTO, ViTAdapter; Mask R-CNN** reaches 0.347 AJI. In both cases, PLUTO outperforms the **ResNet50; Mask R-CNN** baseline.

Disease	Split	Number of Patches	Number of Instances
Breast	Train	82	666
Breast	Heldout	26	281
CRC	Train	40	725
CRC	Heldout	16	474
GI Tract	Train	295	9,083
GI Tract	Heldout	59	2,814

Table 10. Our proprietary Gland segmentation data characterization (includes H&E and IHC).

Disease	Split	Number of Frames	Number of Instances
Breast	Train	26	6,362
Breast	Heldout	17	4,528
CRC	Train	31	6,751
CRC	Heldout	13	2,630
Gastric	Train	29	5,290
Gastric	Heldout	6	1,147
NSCLC	Train	22	7,129
NSCLC	Heldout	19	5,243
Ovarian	Train	33	6,249
Ovarian	Heldout	10	1,933
Esophageal	Train	17	4,213
Esophageal	Heldout	2	291

Table 11. Our proprietary Cell segmentation data characterization (IHC only).

Task	Model Arch.	Inference Patch Size	Embedding (Pooling Method)	Macro F1
H&E Onc. Tissue	PLUTO + MLP	16	CLS (N/A)	0.720
H&E Onc. Tissue	PLUTO + MLP	16	All Patch-Token (Mean) + CLS	0.722
H&E Onc. Tissue	PLUTO + MLP	16	All Patch-Token (Attention)	0.743
H&E Onc. Tissue	PLUTO + MLP	16	All Patch-Token (Attention) + CLS	0.751
H&E Onc. Tissue	CNN (Baseline)	-	-	0.672
IHC Onc. Tissue	PLUTO + MLP	16	CLS (N/A)	0.764
IHC Onc. Tissue	PLUTO + MLP	16	All Patch-Token (Mean) + CLS	0.767
IHC Onc. Tissue	PLUTO + MLP	16	All Patch-Token (Attention)	0.768
IHC Onc. Tissue	PLUTO + MLP	16	All Patch-Token (Attention) + CLS	0.777
IHC Onc. Tissue	CNN (Baseline)	-	-	0.721
H&E IBD Tissue	PLUTO + MLP	16	CLS (N/A)	0.544
H&E IBD Tissue	PLUTO + MLP	16	All Patch-Token (Mean) + CLS	0.551
H&E IBD Tissue	PLUTO + MLP	16	All Patch-Token (Attention)	0.658
H&E IBD Tissue	PLUTO + MLP	16	All Patch-Token (Attention) + CLS	0.688
H&E IBD Tissue	CNN (Baseline)	-	-	0.687

Table 12. Performance on tissue tile classification tasks on our proprietary datasets. On oncology tasks, the CLS token contains enough information to perform well. In all cases, adding Attention improves the macro-F1, with the largest gains in IBD Tissue. There, possibly due to the complexity of the task, attention is necessary for the classifier to learn the relevant context for classification. IBD Tissue is also where the CNN Baseline and the PLUTO models perform most similarly.

Task	Model Arch.	Inference Patch Size	Embedding (Pooling Method)	Macro F1
H&E Onc. Cell	PLUTO + MLP	8	Sub Patch-Token (Mean) + CLS	0.771
H&E Onc. Cell	PLUTO + MLP	8	All Patch-Token (Attention)	0.760
H&E Onc. Cell	PLUTO + MLP	8	All Patch-Token (Attention) + CLS	0.789
H&E Onc. Cell	CNN (Baseline)	-	-	0.749

Table 13. Performance on cell tile classification tasks on our proprietary dataset. We use the mean of the center four patch-token embeddings and concatenate it with the CLS token as the baseline PLUTO embeddings. Adding Attention does not alter performance substantially in this scenario, and all PLUTO models outperform the CNN Baseline.

Disease	Split	Number of Frames	Number of Instances
Breast	Train	41	4,019
Breast	Heldout	23	2,279
CRC	Train	23	2,865
CRC	Heldout	10	1,410
DLBCL	Heldout	2	912
Gastric	Train	9	1,098
Gastric	Heldout	3	394
HCC	Train	6	2,065
HNSCC	Train	1	526
Hepatitis	Train	3	632
IBD	Train	1	778
RCC	Train	4	587
RCC	Heldout	3	905
Ovarian	Train	17	1,995
Ovarian	Heldout	4	456
Prostate	Train	1	254
Prostate	Heldout	2	590
NASH	Train	3	644
NASH	Heldout	2	410
Lung	Train	24	3,859
Lung	Heldout	19	2,685
Esophageal	Heldout	2	893
Leukemia	Train	1	491
Lupus	Train	3	1,085
Bile Duct	Train	3	839
UC	Train	2	774
Other	Heldout	4	1,050

Table 14. Our proprietary Nuclei segmentation data characterization (includes H&E and IHC).